

Amino-acid- and peptide-directed synthesis of chiral plasmonic gold nanoparticles

Hye-Eun Lee^{1,6}, Hyo-Yong Ahn^{1,6}, Jungho Mun², Yoon Young Lee¹, Minkyung Kim³, Nam Heon Cho¹, Kiseok Chang⁴, Wook Sung Kim^{4,5}, Junsuk Rho^{2,3*} & Ki Tae Nam^{1*}

Understanding chirality, or handedness, in molecules is important because of the enantioselectivity that is observed in many biochemical reactions¹, and because of the recent development of chiral metamaterials with exceptional light-manipulating capabilities, such as polarization control^{2–4}, a negative refractive index⁵ and chiral sensing⁶. Chiral nanostructures have been produced using nanofabrication techniques such as lithography⁷ and molecular self-assembly^{8–11}, but large-scale and simple fabrication methods for three-dimensional chiral structures remain a challenge. In this regard, chirality transfer represents a simpler and more efficient method for controlling chiral morphology^{12–18}. Although a few studies^{18,19} have described the transfer of molecular chirality into micrometre-sized helical ceramic crystals, this technique has yet to be implemented for metal nanoparticles with sizes of hundreds of nanometres. Here we develop a strategy for synthesizing chiral gold nanoparticles that involves using amino acids and peptides to control the optical activity, handedness and chiral plasmonic resonance of the nanoparticles. The key requirement for achieving such chiral structures is the formation of high-Miller-index surfaces ($\{hkl\}$, $h \neq k \neq l \neq 0$) that are intrinsically chiral, owing to the presence of ‘kink’ sites^{20–22} in the nanoparticles during growth. The presence of chiral components at the inorganic surface of the nanoparticles and in the amino acids and peptides results in enantioselective interactions at the interface between these elements; these interactions lead to asymmetric evolution of the nanoparticles and the formation of helicoid morphologies that consist of highly twisted chiral elements. The gold nanoparticles that we grow display strong chiral plasmonic optical activity (a dissymmetry factor of 0.2), even when dispersed randomly in solution; this observation is supported by theoretical calculations and direct visualizations of macroscopic colour transformations. We anticipate that our strategy will aid in the rational design and fabrication of three-dimensional chiral nanostructures for use in plasmonic metamaterial applications.

To control the chiral morphology of gold nanoparticles through molecular interactions of amino acids or peptides with high-index surfaces, we devised an aqueous-based, two-step growth method involving organothiols additives. As the first step, low-index-plane-exposed gold nanoparticles of uniform size were synthesized using the well-established seed-mediated method^{23–25}. In the second step, cysteine or cysteine-based peptides with chiral conformations were used to encode chirality into the gold nanoparticles. The molecules were added to the growth solution, in which the pre-synthesized low-index-plane-exposed gold nanoparticles evolved into high-index-plane-exposed nanoparticles as a result of the reduction of Au⁺ ions (see Methods for detailed experimental procedure). Au–S bonding and interactions of other functional groups in the amino acid or peptides are also involved in the nanoparticle growth process. Peptide-sequence-specific interactions have been investigated as a way of controlling the growth of nanomaterials and their optical properties^{26–28}. Changes in growth

components, such as the peptide sequence and concentration, and in seed morphology affect the growth kinetics and induce the dynamic morphological evolution of low-index-plane-exposed gold seed nanoparticles into chiral nanoparticles.

Circular dichroism and scanning electron microscopy (SEM) analyses confirm the synthesis of chiral plasmonic nanoparticles (Fig. 1). Notably, the conformation of the molecule used for synthesis controlled the handedness of the resulting nanoparticles. When L- or D- amino acids were added during the nanoparticle growth process, the nanoparticles that formed had the opposite handedness. Optical responses followed the handedness of nanoparticles. For example, when L-cysteine (L-Cys) and D-cysteine (D-Cys) were used as additives, the associated extinction spectra of the synthesized nanoparticles were identical and depended on only the overall particle size (Extended Data Fig. 1a). However, the measured circular dichroism spectra were inverted with respect to each other, but had the same peak positions, at 569 nm and 699 nm (Fig. 1a). In both the cases, the morphologies of the synthesized nanoparticles were cube-like, with a side length of 150 nm. An interesting feature of the nanoparticles synthesized using L-Cys and D-Cys is that the vertices protrude and the edges, which typically bridge two vertices in a cube, are split into two. As shown in the insets of Fig. 1b, the two split edges for the L-Cys nanoparticles point in opposite directions (one into and the other out of the cube), with a tilt angle of $-\varphi$. In the case of the D-Cys nanoparticles, the split edges were tilted in the opposite direction, at an angle of $+\varphi$ (Fig. 1c). Along the [111] view, the tilted edges protrude as tripods at each vertex of a cube, thereby contributing to the chirality of the synthesized gold nanoparticles (Fig. 1b, right inset). These tripods, which are 40 nm thick and 100 nm long, assemble, making nanometre-scale gaps inside a helicoid cube. The right-handed chiral structures, synthesized using L-Cys as an additive, exhibit increased absorption of left circularly polarized light at 569 nm, whereas the opposite chiro-optical response is observed for the left-handed chiral structures, synthesized using D-Cys. The yield of the chiral nanoparticles using this synthesis approach was about 81% (of a total of 989 nanoparticles) (Extended Data Fig. 1a).

The development of chiral morphology is a result of the different growth rates of the two oppositely chiral high-index planes of gold in the presence of L-Cys or D-Cys. Under our growth conditions, the absence of cysteine resulted in a stellated octahedron, differentiated by $\{321\}$ facets (Fig. 2a, Extended Data Fig. 2a). (The synthesis method reported here can also be used to modify other stellated nanostructures^{29,30}.) We assigned the $\{321\}$ indexing by analysing the relative angles of each edge in transmission electron microscopy (TEM) images (Extended Data Fig. 2c, d). The stellated octahedron has $4/m\bar{3}2/m$ point-group symmetry, defined by 48 identical triangular faces. The $\{321\}$ facets are in the R (clockwise rotation, $(321)^R$) or S (anticlockwise rotation, $(3\bar{2}\bar{1})^S$) conformation, defined by the rotational direction of the low-index planes (or microfacets) (100), (110) and (111), as outlined black in Fig. 2b^{20–22}. In Fig. 2a, the pairs of $\{hkl\}$ planes with R and S conformation (within the rhombus ABA'B') are indicated in purple

¹Department of Materials Science and Engineering, Seoul National University, Seoul, South Korea. ²Department of Chemical Engineering, Pohang University of Science and Technology (POSTECH), Pohang, South Korea. ³Department of Mechanical Engineering, POSTECH, Pohang, South Korea. ⁴R&D Center, LG Display, LG Science Park, Seoul, South Korea. ⁵Department of Electrical Engineering, POSTECH, Pohang, South Korea. ⁶These authors contributed equally: Hye-Eun Lee, Hyo-Yong Ahn. *e-mail: jsrho@postech.ac.kr; nkitae@snu.ac.kr

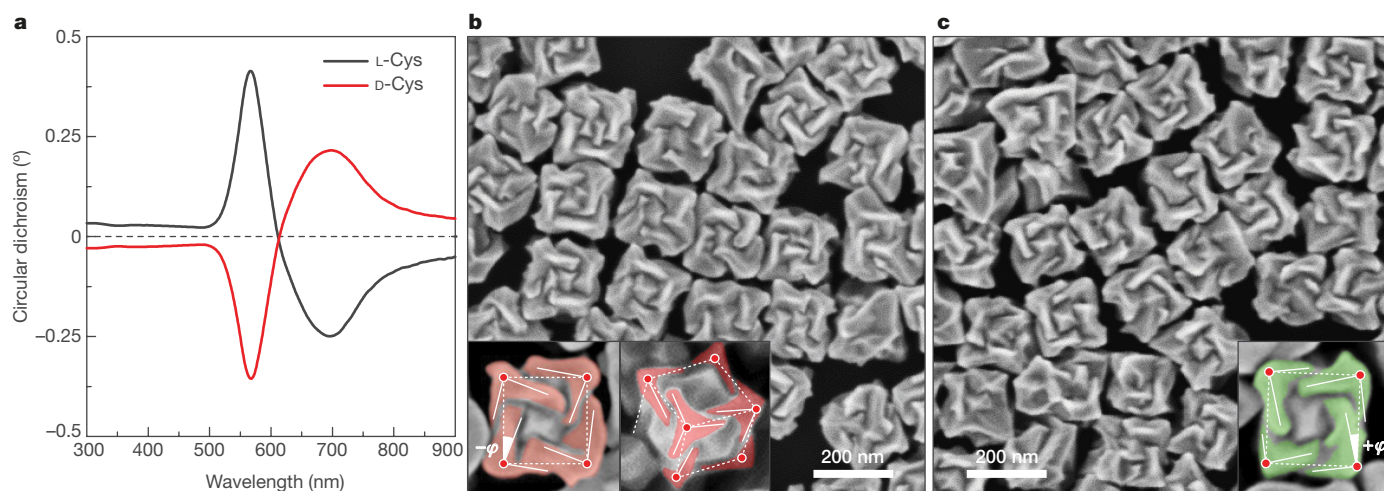


Fig. 1 | Opposite handedness of three-dimensional plasmonic helicoids controlled by cysteine chirality transfer. **a**, Circular dichroism spectra of chiral nanoparticles synthesized using L-Cys (black) and D-Cys (red). **b**, SEM image of L-Cys nanoparticles. The highlighting in the insets illustrates the fact that the edges (solid lines) are tilted by an angle $-\varphi$

with respect to the vertices (red dots) and cubic outline (dashed lines), as viewed along the [100] (left) and [111] (right) directions. **c**, SEM image of D-Cys nanoparticles. The inset highlights the tilted edges (solid lines), cubic outline (dashed lines) and tilt angle ($+\varphi$).

and yellow, respectively. The *R* and *S* triangular regions alternate and their distribution is essentially symmetric and achiral. We observe that the chiral morphologies developed as a result of the shifting and tilting of specific *R*–*S* boundaries. We present a detailed analysis of the time-dependent evolution when using L-Cys as the additive in the following.

The addition of low-index-plane-exposed cube-shaped seeds into the second-step solution containing L-Cys begins the growth. To monitor the evolution of morphology, nanoparticles were grown for different reaction times from 10 min to 120 min. The underlying mechanism of the evolution is most clearly evident in the 20-min case, in which the *g*-factor (see Methods) starts to increase over the next 20 min (Fig. 2c, d, Extended Data Fig. 4d). For clear visualization, the rhombus $ABA'B'$, which consists of two sets of *R* and *S* regions, is displayed schematically (Fig. 2c, d, top) and marked with red dots and dotted white lines in the corresponding SEM images (Fig. 2c, d, bottom). Substantial changes, such as splitting, movement and overgrowth, were found at the *R*–*S* boundaries AC and $A'C$ in the rhombus $ABA'B'$, and the 12 equivalent boundaries changed in the same manner. AC and $A'C$ were both tilted by $-\varphi$ towards the *S* regions and protruded with distortion, as indicated by the red-patterned area and arrows in Fig. 2c, d. In the [111] and [100] directions, the chiral elements formed three- and four-fold symmetry, respectively. As shown in the sequential images of the growth process (Extended Data Fig. 2e, f), the twisted edges continued to thicken, growing laterally and evolving into the final morphology, in which the elongated edges are twisted inwards (Fig. 2e). As the mirror symmetry of the *R* and *S* regions was broken by the distortion, the $4/m\bar{3}2/m$ point-group symmetry of the stellated octahedron changed to 432 symmetry. We therefore designate any nanoparticle with this chiral morphology as a '432 helicoid I'. When using D-Cys as the additive in the second-step solution, the *R*–*S* boundaries AC and $A'C$ are tilted by $+\varphi$ towards the *R* regions, resulting in a 432 helicoid I with opposite chirality.

In high-resolution TEM images (Extended Data Fig. 3a), the steps and terraces on the facets of a chiral nanoparticle at an early stage of growth (20 min) reveal the Cys adsorption on the high-index plane. In addition, the increased adsorption energy, as demonstrated by temperature-programmed desorption and electrochemical desorption studies, suggests that the molecules bind to a high-index surface (Extended Data Fig. 3b, c). N-terminal blocking of L-Cys completely inhibits the formation of chiral particles, and C-terminal blocking reduces the *g*-factor (Extended Data Fig. 5a). These data imply that

the thiol and amine groups bind with the 'kinks' on the {321} facets. This mechanism is also supported by previous studies^{31–33}, which have shown that the relative location of an amine group with respect to a thiol is the main determinant of the different binding affinities to *R* or *S* kink sites. Therefore, the preferred interaction of L-Cys with the {321} planes in the *R* regions leads to slower growth in the vertical direction on the *R* regions than on the *S* regions. For this reason, the *R*–*S* boundary shifts from the *R* to the *S* region, accompanied by asymmetric overgrowth.

The surface coverage of L-Cys is estimated to be 0.01 monolayers ($0.028 \text{ nmol cm}^{-2}$) at the optimal concentration (at which 432 helicoid I exhibits the highest *g*-factor) (Extended Data Fig. 4a–c, Methods). This low coverage seems to be necessary for chiral-selective growth—weak-binding motifs such as amine and carboxylic groups would be interfered with at high concentrations (Extended Data Fig. 4g). In addition, from a screening experiment with several peptide sequences, we found that other functional groups as well as thiol are key to determining the chiral morphology (Methods).

One of the most interesting results of our study is that the addition of L-glutathione (L-GSH) instead of L-Cys or D-Cys induces a completely different chiral morphology, by shifting a different *R*–*S* boundary (Fig. 2f–h). We observe a change in the four outer boundaries of the rhombus $ABA'B'$ instead of in the inner AC and $A'C$ boundaries, as was observed in the case of L-Cys. Note that AC and $A'C$ are convex, whereas BC and $B'C$ are concave. AB and $A'B'$ both expand outwards, while the other boundaries (AB' and $A'B$) move inwards, distorting the boundary of the rhombus $ABA'B'$ (Fig. 2f). Consequently, a pinwheel-like chiral structure with clockwise rotation and four-fold symmetry appears along the [100] direction (Fig. 2g, h). We refer to any nanoparticle with this helicoid morphology as a '432 helicoid II'. A low-magnification SEM image shows uniformly synthesized 432 helicoid II particles (Extended Data Fig. 1b).

The different growth directions of 432 helicoids I and II can be understood at the atomic level by looking at the facets with $(321)^R$ conformation surrounded by those with $(312)^S$ and $(231)^S$ conformation in the [111] direction (Extended Data Fig. 5b–d). $(321)^R$ structures are composed of a (111) terrace and alternating (100) and (110) microfacets. Different orders of (100) and (110) alternation result in opposite chirality, such as $(312)^S$ or $(231)^S$. AC , which is important in 432 helicoid I, is the boundary of $(321)^R$ and $(231)^S$, AB , which is important in 432 helicoid II, is the boundary of $(321)^R$ and $(312)^S$. This property indicates that L-Cys and L-GSH shift the AC boundary in the $[\bar{1}01]$

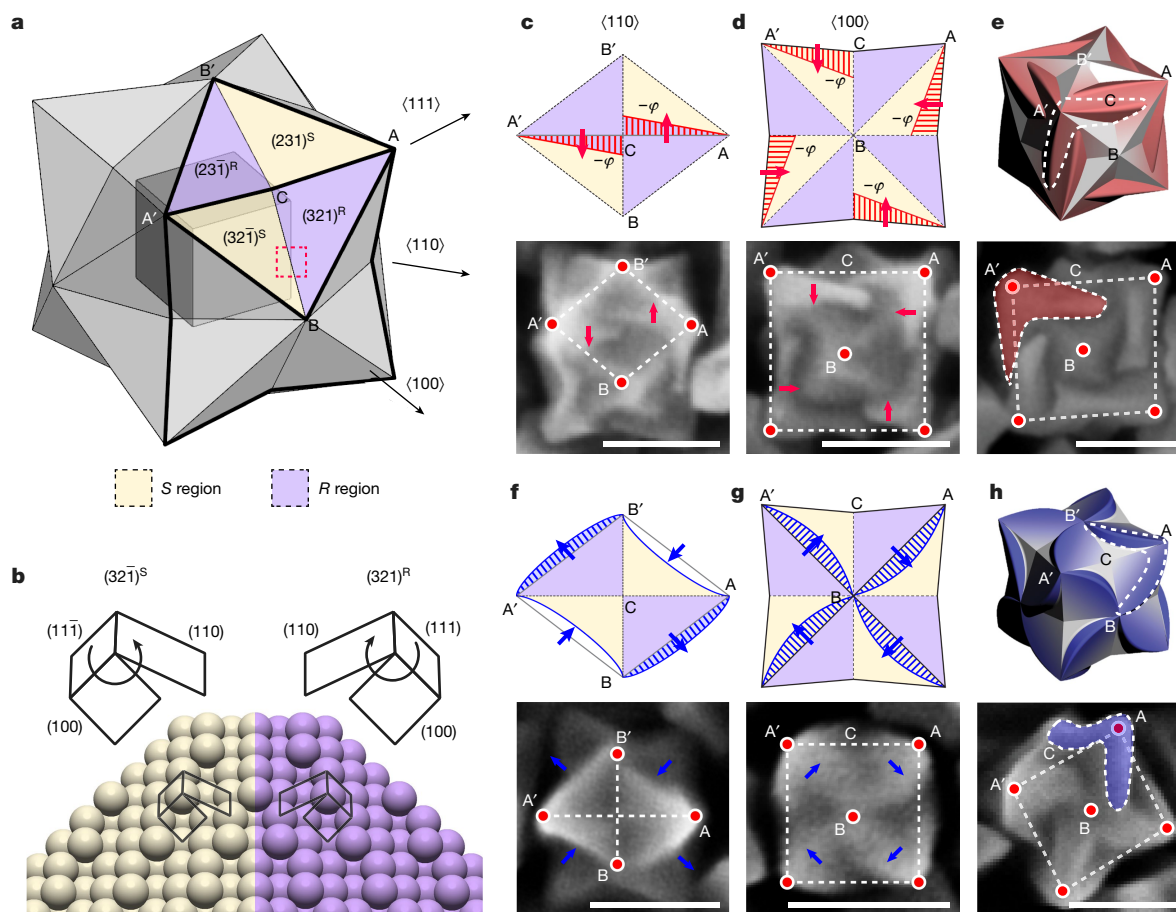


Fig. 2 | Mechanism of chirality evolution through the interplay between the enantioselective binding of molecules and the asymmetric growth of high-index facets. **a**, Schematic of a stellated octahedron, differentiated by high-index facets consisting of $\{321\}^S$ (S region, yellow) and $\{321\}^R$ (R region, purple) configurations. The vertices of the $[111]$, $[100]$ and $[110]$ directions are indicated as A, B and C, respectively; A' and B' refer to the symmetric points of A and B, respectively. **b**, Comparison of the atomic arrangement of the $\{321\}^R$ and $\{321\}^S$ gold surfaces for region indicated by the red dotted box in **a**. The conformation at 'kink' sites is defined by the rotational direction of low-index microfacets in the sequence $(111) \rightarrow (100) \rightarrow (110)$: clockwise, R region; anticlockwise, S region. **c**, **d**, Schematics (top) and SEM images (bottom) of R–S pairs

showing the morphological development of 432 helicoid I in the presence of L-Cys, as viewed along the $[110]$ (**c**) and $[100]$ (**d**) directions. Newly developed boundaries are indicated as red patterned areas with arrows; each vertex is marked on the corresponding SEM image. **e**, Three-dimensional model (top) and SEM image (bottom) of the final chiral shape. The newly formed R region is coloured red and the chiral element is indicated by the dashed outline. The red shaded region in **e** is equivalent to the red patterned areas in **c** and **d**. **f**, **g**, Morphological development of 432 helicoid II in the presence of L-GSH. **h**, The corresponding final chiral shape. The newly formed boundaries and the pinwheel-like chiral elements of the final shape are coloured blue. Scale bars, 100 nm.

direction and the \overline{AB} boundary in the $[01\overline{1}]$ direction, respectively. On the $\{321\}$ surfaces, the gold atoms attach to the (100) and (110) microfacets at the kink, generating a new kink. We propose that the orientation of the Cys or GSH molecule that is adsorbed could determine the specific growth direction of the kinks. Owing to the larger molecular size, GSH seems to interact with multiple kinks, whereas Cys interacts with only a single kink^{32,33}. We believe that the enantioselective interaction of L-GSH also benefits from the flexibility of the γ -peptide linkage, as supported by experiments with other GSH derivatives (Extended Data Fig. 5e). Calculations based on density functional theory and molecular dynamics are needed to identify other peptide sequences that affect single or multiple R–S boundaries and twist them multi-dimensionally.

The strongest optical activity among the nanoparticles that we synthesized was displayed by those that were synthesized using an octahedral seed instead of a cubic seed and therefore exhibit another type of chiral structure; we designate any such nanoparticle as a '432 helicoid III'. 432 helicoid III nanoparticles have pinwheel-like structures—consisting of four highly curved arms of increasing width—on each of the six faces of the cubic geometry (Fig. 3a, b, Extended Data Fig. 6a). Compared to 432 helicoids I and II, the chiral elements in 432 helicoid III are twisted with larger curvature and the gaps between them are

carved more deeply in the central direction. Imaging after ion milling using helium-ion microscopy shows the curved surfaces located inside the gaps (Extended Data Fig. 6b). From the depth and curvature information, we construct a three-dimensional model to assign the Miller index at each location (Extended Data Fig. 6c, d). The strong circular dichroism signal of this structure (Fig. 3c) is largely attributed to the highly twisted chiral structures and is consistent with the simulation results (Fig. 3d). The g -factor of 432 helicoid III is approximately 0.2 at 622 nm, which is roughly ten and three times larger than that of 432 helicoids I and II, respectively (Fig. 3e). The g -factors of various chiral nanostructures are compared in Extended Data Table 1. The g -factor of 432 helicoid III is larger than that of any other chiral nanostructure fabricated using bottom-up approaches. The exceptionally strong chiro-optical properties of 432 helicoid III may have resulted from the high-order plasmonic modes of large continuous chiral particles (Extended Data Fig. 7). The intensity difference for the electric and magnetic near-fields (Fig. 3f) is consistent with the macroscopic asymmetric response of 432 helicoid III to circularly polarized light. Interestingly, in contrast to a symmetric sphere, the induced magnetic dipole moment of 432 helicoid III cannot be perpendicular to the induced electric dipole moment. We also find that several other structural changes, such as edge length, gap width, gap depth, gap angle

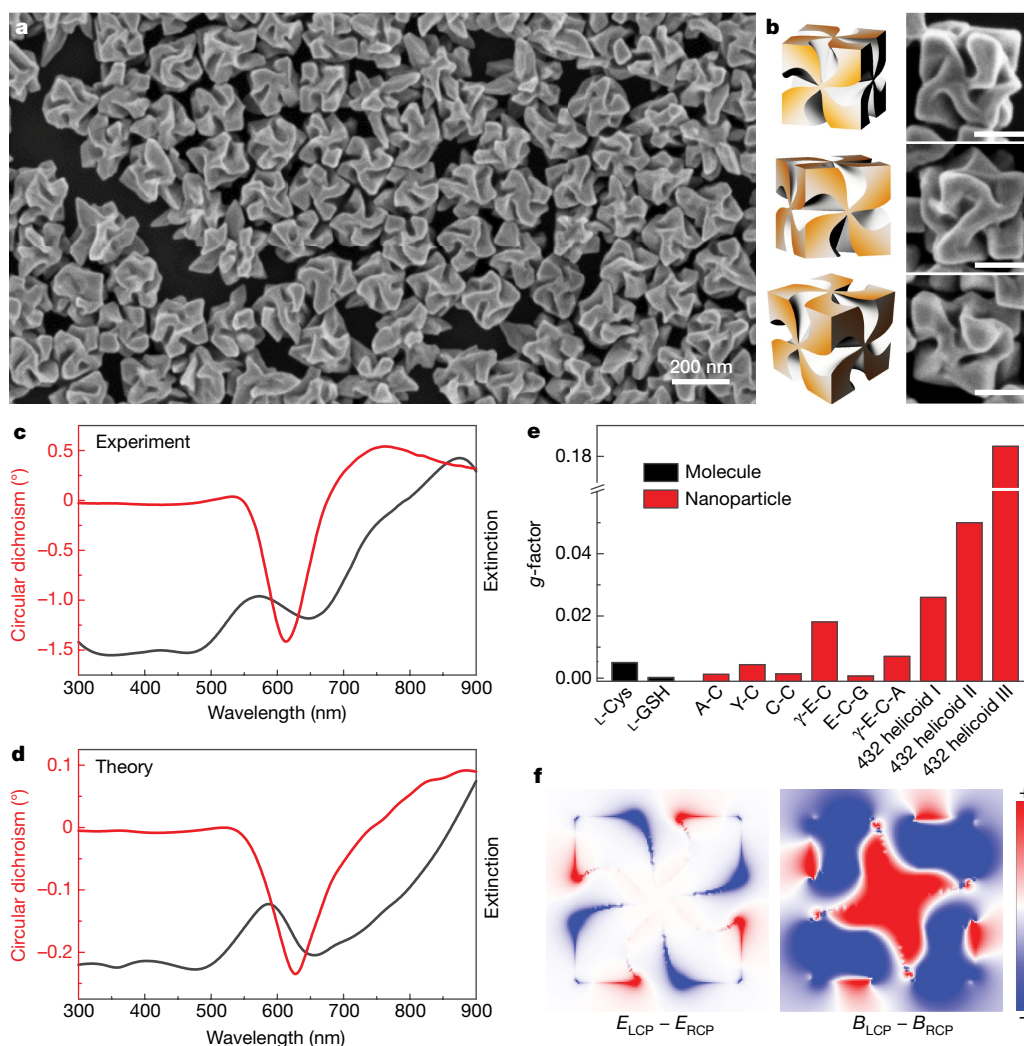


Fig. 3 | Morphology and optical activity of 432 helicoid III. **a**, SEM image of 432 helicoid III nanoparticles evolved from an octahedral seed. **b**, Three-dimensional models (left) and corresponding SEM images (right) of 432 helicoid III oriented in various directions. Scale bars, 100 nm. **c**, **d**, Experimental (**c**) and theoretical (**d**; based on a finite-difference time-domain method) circular dichroism and extinction spectra of 432 helicoid III. **e**, Comparison of the dissymmetry g -factors of the synthesized helicoid structures and other nanoparticles (SEM images are shown in Extended Data Fig. 5e, f). A-C, L-alanyl-L-cysteine; Y-C, L-tyrosyl-L-cysteine; C-C, L-cysteinyl-L-cysteine; γ -E-C, γ -L-glutamyl-L-cysteine; E-C-G, L-glutamyl-L-cysteinyl-glycine; γ -E-C-A, γ -L-glutamyl-L-cysteinyl-L-alanine. **f**, Theoretical calculation of the dependence of local electromagnetic fields on the handedness of circularly polarized light. The asymmetric responses of the electric (left; E) and magnetic (right; B) fields are displayed by the differences in these fields under excitation by left circularly polarized (LCP) and right circularly polarized (RCP) light. The colour scale indicates the magnitude of the field difference, with red (blue) indicating a positive (negative) difference.

and curvature, affect the chiro-optical activity of the nanoparticles (Extended Data Figs 8, 9, Methods).

As a result of the large g -factor of the helicoid nanoparticles, a macroscopically distinguishable change in their colour is possible by controlling the polarization. The circular dichroism spectrum and the corresponding optical rotatory dispersion spectrum for 432 helicoid III are presented in Fig. 4a, and the output polarization state was measured directly at four wavelengths using linearly polarized incident light (Fig. 4b). The largest ellipticity ($\chi = -28.7^\circ$, left circular polarization) was observed at 635 nm and the azimuthal rotation (ψ) changed gradually from -7.9° to $+29^\circ$ as the wavelength was increased. The conversion from linearly to elliptically polarized light by 432 helicoid III is clear under cross-polarized conditions. Although the achiral nanoparticles did not exhibit any transmission (Fig. 4c, left), a solution of 432 helicoid III nanoparticles showed bright yellow cross-polarized transmission, which reflects a pronounced polarization-rotating ability at visible wavelengths (Fig. 4c, right). Further, we confirmed the isotropic response and Lorentz reciprocity of the nanoparticles (Extended Data Fig. 10a, b). Changing the size of 432 helicoid III nanoparticles by controlling the initial seed concentration caused a resonance shift of the

resulting nanoparticles, with λ_{\max} (the wavelength at which the maximum g -factor is observed) increasing from 552 nm to 668 nm (Fig. 4d, Extended Data Fig. 10c). This modification also enabled gradual tuning of the transmitted colours under cross-polarized conditions (0° , dotted box in Fig. 4e). In addition, rotation of the analyser reversibly generated various transmitted colours, thereby providing a versatile method of colour modulation that reflects the optical rotatory dispersion response (Fig. 4e, Extended Data Fig. 10d, Supplementary Video 1). In contrast to the symmetric pattern for achiral nanoparticles, the colour transition of 432 helicoid III was continuous and asymmetric (Fig. 4e), forming elliptical traces in the chromaticity diagram (Extended Data Fig. 10e–h). The colour transformation of 432 helicoid III was dynamic and covered a wide range of colours.

We envision that the biomolecular approach presented here for the evolution of chirality in a plasmonic helicoid has technological potential for the development of biologically responsive and tunable metamaterials. Using this approach, chiral elements were arranged within cube-like structures with a side length of only about 100 nm, resulting in three-dimensional, angle-insensitive plasmonic metamaterials. We believe that conformation control using long peptides or other chiral

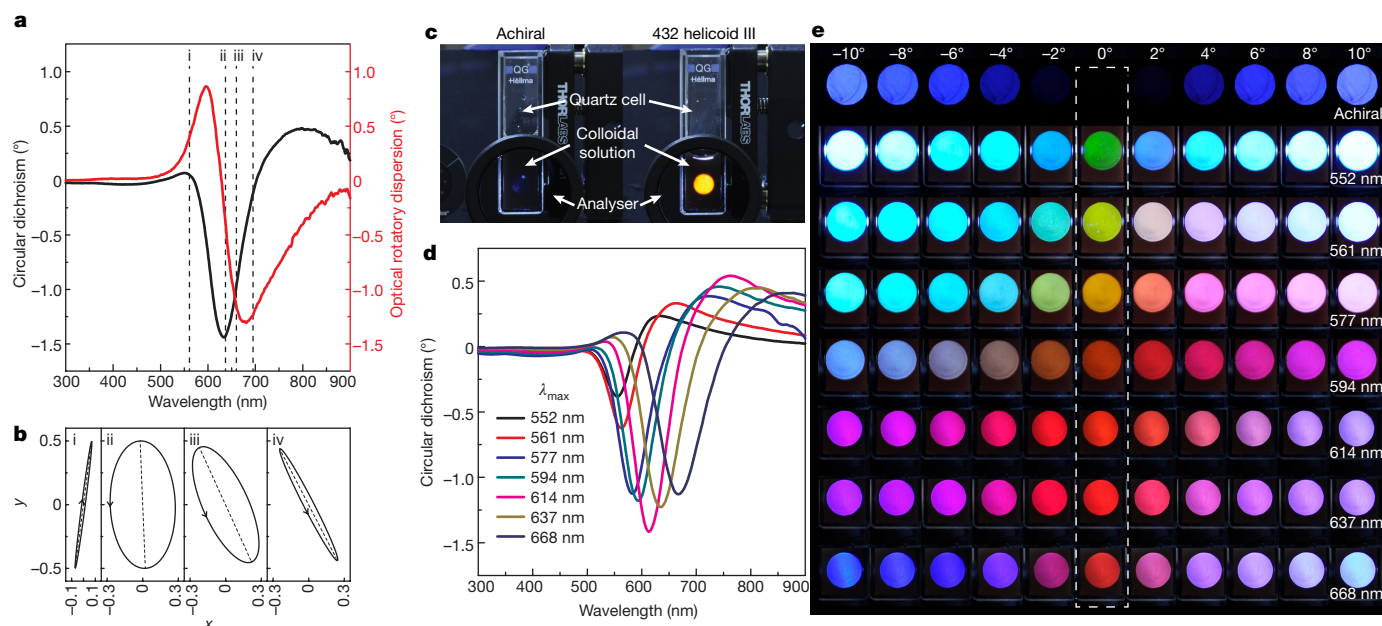


Fig. 4 | Visible light polarization control by 432 helicoid III solution. **a**, Circular dichroism and optical rotatory dispersion spectra of 432 helicoid III. **b**, Output polarization states measured at the wavelengths indicated in **a**: 561 nm (i), 635 nm (ii), 658 nm (iii) and 690 nm (iv). The polarization ellipses at each wavelength expressed in terms of the ellipticity (χ) and azimuthal rotation (ψ) are: $\chi = 1.7^\circ$ and $\psi = -7.9^\circ$ at 561 nm; $\chi = -28.7^\circ$ and $\psi = 2.6^\circ$ at 635 nm; $\chi = -20.7^\circ$ and $\psi = 26.6^\circ$ at 658 nm; and $\chi = -4.8^\circ$ and $\psi = 29.0^\circ$ at 690 nm (x and y are the horizontal and vertical components of the electric-field vector). **c**, Photographs of achiral (left) and 432 helicoid III (right) solutions, showing the light transmitted

under cross-polarized conditions. **d**, Circular dichroism spectra of 432 helicoid III for different values of λ_{\max} (the wavelength of the maximum g -factor). Seven spectra were obtained from differently sized 432 helicoid III nanoparticles with various resonance peaks (552 nm, 561 nm, 577 nm, 594 nm, 614 nm, 637 nm and 668 nm). **e**, Polarization-resolved colours of light transmitted through seven different 432 helicoid III solutions with different λ_{\max} values (shown on the right) and an achiral nanoparticle solution (top row). The rotational angle of the analyser was increased from -10° (left-most) to 10° (right-most) (see Methods). An angle of 0° , indicated by the dashed box, represents cross-polarized conditions.

biomolecules will enable the synthesis of other sets of chiral symmetry groups. Further, insights from this study could provide theoretical guidelines for designing artificial chirality and chiro-optical properties for active colour displays, holography, reconfigurable switching, chirality sensing and all-angle negative-refractive-index materials.

Online content

Any Methods, including any statements of data availability and Nature Research reporting summaries, along with any additional references and Source Data files, are available in the online version of the paper at <https://doi.org/10.1038/s41586-018-0034-1>.

Received: 29 May 2017; Accepted: 26 February 2018;
Published online 18 April 2018.

- Hazen, R. M. & Sholl, D. S. Chiral selection on inorganic crystalline surfaces. *Nat. Mater.* **2**, 367–374 (2003).
- Gansel, J. K. et al. Gold helix photonic metamaterial as broadband circular polarizer. *Science* **325**, 1513–1515 (2009).
- Meinzer, N., Barnes, W. L. & Hooper, I. R. Plasmonic meta-atoms and metasurfaces. *Nat. Photon.* **8**, 889–898 (2014).
- Zhang, S. et al. Photoinduced handedness switching in terahertz chiral metamolecules. *Nat. Commun.* **3**, 942 (2012).
- Pendry, J. B. A chiral route to negative refraction. *Science* **306**, 1353–1355 (2004).
- Hendry, E. et al. Ultrasensitive detection and characterization of biomolecules using superchiral fields. *Nat. Nanotechnol.* **5**, 783–787 (2010).
- Soukoulis, C. M. & Wegener, M. Past achievements and future challenges in the development of three-dimensional photonic metamaterials. *Nat. Photon.* **5**, 523–530 (2011).
- Ma, W. et al. Chiral inorganic nanostructures. *Chem. Rev.* **117**, 8041–8093 (2017).
- Kuzyk, A. et al. DNA-based self-assembly of chiral plasmonic nanostructures with tailored optical response. *Nature* **483**, 311–314 (2012).
- Kuzyk, A. et al. Reconfigurable 3D plasmonic metamolecules. *Nat. Mater.* **13**, 862–866 (2014).
- Lee, H.-E., Ahn, H.-Y., Lee, J. & Nam, K. T. Biomolecule-enabled chiral assembly of plasmonic nanostructures. *ChemNanoMat* **3**, 685–697 (2017).
- Kühnle, A., Linderth, T. R., Hammer, B. & Besenbacher, F. Chiral recognition in dimerization of adsorbed cysteine observed by scanning tunnelling microscopy. *Nature* **415**, 891–893 (2002).

- Switzer, J. A., Kothari, H. M., Poizot, P., Nakanishi, S. & Bohannon, E. W. Enantiospecific electrodeposition of a chiral catalyst. *Nature* **425**, 490–493 (2003).
- Horvath, J. D., Koritnik, A., Kamakoti, P., Sholl, D. S. & Gellman, A. J. Enantioselective separation on a naturally chiral surface. *J. Am. Chem. Soc.* **126**, 14988–14994 (2004).
- Xiao, W. et al. Microscopic origin of chiral shape induction in achiral crystals. *Nat. Chem.* **8**, 326–330 (2016).
- Sanchez, C., Arribart, H. & Guille, M. M. G. Biomimetic and bioinspiration as tools for the design of innovative materials and systems. *Nat. Mater.* **4**, 277–288 (2005).
- Weissbuch, I., Addadi, L., Lahav, M. & Leiserowitz, L. Molecular recognition at crystal interfaces. *Science* **253**, 637–645 (1991).
- Che, S. et al. Synthesis and characterization of chiral mesoporous silica. *Nature* **429**, 281–284 (2004).
- Orme, C. A. et al. Formation of chiral morphologies through selective binding of amino acids to calcite surface steps. *Nature* **411**, 775–779 (2001).
- McFadden, C. F., Cremer, P. S. & Gellman, A. J. Adsorption of chiral alcohols on “chiral” metal surfaces. *Langmuir* **12**, 2483–2487 (1996).
- Ahmadi, A., Attard, G., Feliu, J. & Rodes, A. Surface reactivity at “chiral” platinum surfaces. *Langmuir* **15**, 2420–2424 (1999).
- Sholl, D. S., Asthagiri, A. & Power, T. D. Naturally chiral metal surfaces as enantiospecific adsorbents. *J. Phys. Chem. B* **105**, 4771–4782 (2001).
- Sau, T. K. & Murphy, C. J. Room temperature, high-yield synthesis of multiple shapes of gold nanoparticles in aqueous solution. *J. Am. Chem. Soc.* **126**, 8648–8649 (2004).
- Ahn, H.-Y., Lee, H.-E., Jin, K. & Nam, K. T. Extended gold nano-morphology diagram: synthesis of rhombic dodecahedra using CTAB and ascorbic acid. *J. Mater. Chem. C* **1**, 6861–6868 (2013).
- Lee, H.-E. et al. Concave rhombic dodecahedral Au nanocatalyst with multiple high-index facets for CO₂ reduction. *ACS Nano* **9**, 8384–8393 (2015).
- Dickerson, M. B., Sandhage, K. H. & Naik, R. R. Protein- and peptide-directed syntheses of inorganic materials. *Chem. Rev.* **108**, 4935–4978 (2008).
- Slocik, J. M., Govorov, A. O. & Naik, R. R. Plasmonic circular dichroism of peptide-functionalized gold nanoparticles. *Nano Lett.* **11**, 701–705 (2011).
- Coppage, R. et al. Determining peptide sequence effects that control the size, structure, and function of nanoparticles. *ACS Nano* **6**, 1625–1636 (2012).
- Liu, H. et al. Stellated Ag-Pt bimetallic nanoparticles: an effective platform for catalytic activity tuning. *Sci. Rep.* **4**, 3969 (2014).
- Weiner, R. G. & Skrabalak, S. E. Metal dendrimers: synthesis of hierarchically stellated nanocrystals by sequential seed-directed overgrowth. *Angew. Chem. Int. Ed.* **54**, 1181–1184 (2015).

31. Kühnle, A., Linderoth, T. R. & Besenbacher, F. Enantiospecific adsorption of cysteine at chiral kink sites on Au(110)-(1×2). *J. Am. Chem. Soc.* **128**, 1076–1077 (2006).
32. Greber, T., Slijvančanin, Z., Schillinger, R., Wider, J. & Hammer, B. Chiral recognition of organic molecules by atomic kinks on surfaces. *Phys. Rev. Lett.* **96**, 056103 (2006).
33. Schillinger, R., Slijvančanin, Z., Hammer, B. & Greber, T. Probing enantioselectivity with x-ray photoelectron spectroscopy and density functional theory. *Phys. Rev. Lett.* **98**, 136102 (2007).

Acknowledgements This research was supported by a Seoul National University research grant in 2015, the LG Display under LGD-SNU Incubation Program, the Creative Materials Discovery Program (2017M3D1A1039377), which is funded by the National Research Foundation (NRF) under the Ministry of Science, ICT and Future Planning (MSIP), South Korea, and the KIST-SNU Joint Research Program (0543-20180021). K.T.N. acknowledges financial supports from the Global Frontier R&D Program of the Center for Multiscale Energy System (2012M3A6A7054855), which is funded by the NRF-MSIP, South Korea. J.R. acknowledges financial support from the Engineering Research Center Program of the Center for Optically-assisted Mechanical Systems (2015R1A5A1037668) and the Global Frontier R&D Program of the Center for Advanced Meta-Materials (2014M3A6B3063708), which is funded by the NRF-MSIP, South Korea. H.-Y.A. and M.K. are grateful to the Global PhD Fellowship Program (2014H1A2A1020809 and 2017H1A2A1043204, respectively), which is funded by the NRF-MSIP,

South Korea. J.R. thanks T. Liedl (Ludwig Maximilian University of Munich) and N. Liu (University of Heidelberg) for discussions.

Reviewer information *Nature* thanks L. M. Liz-Marzán and the other anonymous reviewer(s) for their contribution to the peer review of this work.

Author contributions K.T.N. and J.R. conceived the idea. H.-E.L., H.-Y.A., N.H.C. and Y.Y.L. synthesized and characterized the materials. J.M., M.K. and J.R. performed the numerical simulations and analysed the data. H.-E.L., H.-Y.A., K.C. and W.S.K. conducted the optical characterization of the materials. All authors discussed the experiments and contributed to writing the manuscript. J.R. guided the numerical simulations and optical measurements. K.T.N. guided all aspects of the work.

Competing interests The authors declare no competing interests.

Additional information

Extended data is available for this paper at <https://doi.org/10.1038/s41586-018-0034-1>.

Supplementary information is available for this paper at <https://doi.org/10.1038/s41586-018-0034-1>.

Reprints and permissions information is available at <http://www.nature.com/reprints>.

Correspondence and requests for materials should be addressed to J.R. or K.T.N.

Publisher's note: Springer Nature remains neutral with regard to jurisdictional claims in published maps and institutional affiliations.

METHODS

Chemicals. Hexadecyltrimethylammonium bromide (CTAB, 99%), L-ascorbic acid (AA, 99%) and tetrachloroauric(III) trihydrate (HAuCl₄·3H₂O, 99.9%) were purchased from Sigma-Aldrich. L-cysteine hydrochloride monohydrate (99%, TCI), D-cysteine hydrochloride monohydrate (99%, TCI), L-cysteine ethyl ester hydrochloride (99%, TCI), N-acetyl-L-cysteine (98%, TCI), L-glutathione (γ-E-C-G, 98%, Sigma-Aldrich), L-glutathione ethyl ester (90%, Sigma-Aldrich) and γ-L-glutamyl-L-cysteine (γ-E-C, 80%, Sigma-Aldrich) were obtained commercially and used without further purification. Di- and tri-peptides, L-alanyl-L-cysteine (A-C, > 98%), L-prolyl-L-cysteine (P-C, > 98%), L-cysteinyll-L-cysteine (C-C, > 98%), L-tyrosyl-L-cysteine (Y-C, > 98%), L-glutamyl-L-cysteinyll-glycine (E-C-G, > 98%) and γ-L-glutamyl-L-cysteinyll-L-alanine (γ-E-C-A, > 98%) were provided by GenScript and prepared in hydrochloride salt form before use. All aqueous solutions were prepared using high-purity deionized water (18.2 MΩ cm⁻¹).

Synthesis of chiral nanoparticles. Cubic and octahedral seeds were synthesized as reported previously^{24,34}. Before use, both types of seed nanoparticle were centrifuged (6,708g, 150 s) twice and dispersed in aqueous CTAB (1 mM) solution. In a typical synthesis, a growth solution was prepared by adding 0.8 ml of 100 mM CTAB and 0.2 ml of 10 mM gold chloride trihydrate into 3.95 ml of deionized water to form an [AuBr₄]⁻ complex. Au³⁺ was then reduced to Au⁰ by the rapid injection of 0.475 ml of 100 mM AA solution. The growth of chiral nanoparticles was initiated by adding 5 μl of amino acid or peptide solution and 50 μl of seed solution into the growth solution. For the preparation of 432 helicoid I, cubic seed solution was added to the growth solution and then, after a 20-min incubation, 100 μM cysteine was added. To prepare 432 helicoid II, 2 mM glutathione was added to the growth solution, followed by the addition of cubic seed solution. To prepare 432 helicoid III, 5 mM glutathione was added to the growth solution, followed by the addition of octahedral seed solution. The growth solution was placed in a 30 °C bath for 2 h, and the pink solution gradually became blue with large scattering. The solution was centrifuged twice (1,677g, 60 s) to remove unreacted reagents and was re-dispersed in a 1 mM CTAB solution for further characterization.

Characterization. Extinction and circular dichroism (CD) spectra were obtained using a J-815 spectropolarimeter instrument (JASCO), and optical rotatory dispersion (ORD) spectra were measured using an additional ORD attachment. To check the Lorentz reciprocity, we prepared solutions of nanoparticles and particles attached on the substrate. The CD spectrum of each sample condition was measured in the forwards and backwards directions by changing the direction of the sample relative to the incident light.

Kuhn's dis-symmetry factor (*g*-factor) is a dimensionless quantity that is useful for quantitative comparisons of chiro-optical properties among different systems and was calculated from the measured extinction and CD values using:

$$g\text{-factor} = 2 \frac{A_L - A_R}{A_L + A_R} \times \frac{CD}{\text{extinction}}$$

SEM images were taken with a SIGMA system (Zeiss). TEM images were captured using a JEM-3000F system (JEOL).

The polarization-rotating ability of 432 helicoid III was evaluated from polarization-state measurements using an optical configuration consisting of a laser source, iris, linear polarizer, quarter-wave plate, sample and polarimeter. The output polarization state was measured using a PAX5710VIS-T rotating-wave plate Stokes polarimeter (Thorlabs). Laser sources with centre wavelengths of 561 nm (CNI MGL-FN-561, DPSS Laser), 635 nm (Hitachi HL6321G laser diode), 658 nm (Hitachi HL6501MG laser diode) and 690 nm (Hitachi HL6738MG laser diode) were used. For the measurements, a solution of randomly dispersed 432 helicoid III nanoparticles was added to a quartz cell with a path length of 10 mm, and was then irradiated with a vertically polarized incident beam. A quarter-wave plate was used with a linear polarizer to compensate for any polarization interference caused by other optical parts of the system.

Macroscopic colour changes in transmitted light were detected by polarization-resolved transmission measurements with an optical configuration consisting of a white-light illumination source, iris, linear polarizer, sample, linear polarizer (analyser) and digital camera. The sample was placed between two crossed linear polarizers (0° represents cross-polarized conditions) and was irradiated with a collimated cold white-light source. The angle of the analyser was changed from -10° (clockwise) to +10° (anticlockwise) in steps of 1° from the orthogonal configuration, which enables different wavelengths of light to propagate, rendering different colours of transmitted light. While rotating the analyser, the colour transition of the transmitted light was observable by the naked eye and was recorded with a digital camera (D90, Nikon).

Quantification of amino acids and peptides. To quantify the amount of Cys and GSH on the 432 helicoids I and II, a thiol-selective dye-based fluorometric assay was performed. After complete growth in growth solution (100 nM L-Cys

for 432 helicoid I and 2.5 μM L-GSH for 432 helicoid II), the chiral nanoparticles were centrifuged and washed three times to remove the remaining chemicals in solution except the molecules adsorbed on the nanoparticle surface. By adding NaBH₄ to the nanoparticle solution, the reductive desorption reaction of adsorbed thiolate molecules (Au-SR) started immediately, and free thiol molecules (RS⁻) were released to the solution as follows: Au-SR + e⁻ → Au + RS⁻ (Extended Data Fig. 4a)^{35,36}. The final concentration of NaBH₄ was 25 mM and the final volume of the solution was fixed to 100 μl. After 5 min of incubation, the nanoparticles were centrifuged again and clear supernatant solutions containing the released Cys or GSH molecules were collected and incubated for 1 day in 25 °C to decompose the remaining NaBH₄.

Quantification of Cys and GSH on the 432 helicoids I and II was carried out by using thiol-selective dye (Thiol detection assay kit, Cayman Chemical, 700340). The sample was diluted in the reaction buffer (10 mM phosphate buffer with 1 mM EDTA, pH 7.4). The thiol-selective dye reacted spontaneously with the free thiol of Cys or GSH in the sample solution, producing a fluorescent derivative (Extended Data Fig. 4a). The fluorescence signal of the sample was recorded by using an excitation wavelength of 405 nm and an emission wavelength of 535 nm. For the relative quantification, the standard solution was prepared under the same conditions and measured in the concentration range 0–5 μM. The standard concentration curve showed good linearity, with R² = 0.999 (Extended Data Fig. 4b). The quantified amounts of Cys and GSH on the surface of 432 helicoids I and II were 98.9 ± 22.6 pmol and 280.2 ± 90.2 pmol, respectively.

The adsorption amount of GSH during the synthesis of 432 helicoid II was monitored over time (Extended Data Fig. 4e). To stop the growth at different stages, the particles were centrifuged out every 10 min. After the centrifugation was repeated three times to remove the remaining chemicals, the quantification experiment for GSH was performed as described above.

Calculation of surface coverage. To convert the measured concentration of molecules to the surface coverage, we estimated the total surface area of the 432 helicoid I and II samples. According to extinction measurements for the seed nanoparticles, the total number of nanoparticles in each sample batch was measured to be N_{NP} = 1.53 × 10⁹ ml⁻¹. The surface area of a single 432 helicoid I nanoparticle was A_{NP,H1} = 2.31 × 10⁻⁹ cm², and that of helicoid II was A_{NP,H2} = 1.78 × 10⁻⁹ cm², approximated from the schematic three-dimensional models in Extended Data Fig. 1. Therefore, the total surface area of the nanoparticles in each sample were

$$A_{\text{total}} = N_{\text{NP}} A_{\text{NP}}, \quad A_{\text{total,H1}} = 3.53 \text{ cm}^2, \quad A_{\text{total,H2}} = 2.72 \text{ cm}^2$$

The surface coverage of Cys and GSH in 432 helicoids I and II was calculated from the quantification results and the estimated total surface area of the nanoparticle samples, as shown in Extended Data Fig. 4c. The surface density of Cys and GSH was 0.028 nmol cm⁻² and 0.103 nmol cm⁻², respectively. These values correspond to 0.01 and 0.22 monolayers, respectively, calculated from the reported maximum coverage^{37,38}. On the basis of the surface density estimate, the average intermolecular distance for Cys and GSH is expected to be 2.5 nm and 1.3 nm, respectively. Therefore, we conclude that, under optimized conditions, both molecules have enough room to bind multiple functional groups, as is necessary for enantioselective recognition.

Adsorption study of Cys and GSH on {321} nanoparticles. To compare adsorption kinetics, we measured the amount of adsorbed Cys and GSH on {321} nanoparticles. The {321} nanoparticles were incubated in Cys and GSH solution with different concentrations from 0.5 μM to 10 μM. After 2 h of incubation, the nanoparticles were centrifuged and the clear supernatant solutions that contained the remaining molecules were collected for quantification using thiol-specific dye. The adsorbed amount was calculated by subtracting the measured supernatant concentration from the initial concentration (Extended Data Fig. 4f). Given the concentration, a larger amount of Cys was attached to the high-indexed surface compared to GSH. In addition, a similar trend is reflected in the formation of chiral morphology. Owing to this fast loading of Cys, only 0.1 μM is required for 432 helicoid I, whereas molecules that are 25 times larger are needed for 432 helicoid II to achieve a chiral morphology (Extended Data Fig. 4g, h).

Effects of functional group on chiral morphology. We investigated the effects of functional groups on the resulting morphology of the gold nanoparticles to further understand the amino acid and peptide interactions with the gold surface at a molecular level (Extended Data Fig. 5). The N terminus of the amino acid or peptide that was added was a critical parameter in determining the chiral shape. For example, blocking an amine group in L-Cys greatly reduced chirality (Extended Data Fig. 5a). Different N-terminal sequences modified the morphology and texture of the gold nanoparticle surface considerably. We examined several dipeptides with N-terminal modifications of alanine, proline, cysteine and tyrosine (Extended Data Fig. 5f). The morphology of the resulting nanoparticles was very dependent on the peptide sequence. Such substantial morphological differences may arise from alterations in the binding sites and the spatial arrangement of functional

groups that are imparted by dipeptide side chains. Compared to Cys, GSH has an elongated N terminus owing to the specific γ -Glu group. When γ -Glu is replaced with α -Glu (E-C-G; Extended Data Fig. 5e), the chiral morphology was noticeably degraded. In addition, nanoparticle synthesis using γ -E-C produced a different morphology with a certain level of chirality, whereas other dipeptide cases resulted in achiral morphologies (Extended Data Fig. 5f). These results support the idea that the γ -Glu group has an important role in the evolution of chirality.

In addition to the N-terminal modification, substitution of the C terminus resulted in different types of shape evolution owing to changes in the spatial arrangement of functional groups related to the oriented attachment of amino acids and peptides^{12,31}. When L-Cys ethyl ester with a blocked carboxylic acid group was used in the synthesis, the g -factor was reduced by a factor of approximately ten (Extended Data Fig. 5a). Blocking of the C-terminal carboxylic acid of L-GSH (γ -E-C-G) generated only achiral structures (Extended Data Fig. 5e). In addition, a different chiral morphology was developed by replacing Gly with Ala, probably as a result of the steric hindrance near the C-terminal side. According to a previous report³⁹, the -COOH of the Gly moiety in GSH is involved in binding onto the gold surface, along with the thiol and amine groups. The different chiral structure that is induced by the exchange of sequence at the C terminus suggests that more diversified chiral structures may be synthesized by changing the C-terminal sequence (Extended Data Fig. 5e).

Temporal evolution of chiral nanoparticles. The different molecular features of Cys and GSH collectively influenced the morphological development and thus led to notable changes in the final chiral morphology. To monitor the evolution of chirality, the growth reaction was stopped at different stages by centrifugation, after which we performed three repetitions of washing, re-dispersion and centrifugation to remove the remaining chemicals. To obtain a detailed comparison of chiral evolution, we analysed the temporal growth of 432 helicoids I and II in terms of SEM (Extended Data Fig. 2e, f), g -factor (Extended Data Fig. 4d) and the amount of GSH in a nanoparticle (Extended Data Fig. 4e). —

In the case of 432 helicoid I, the AC and A'C boundaries between the R and S planes started to develop and shift slightly to the S-plane direction, forming the split edges (stage I). In stage I, the g -factor is still low because the chiral components have not developed yet. After 20 min, protruded edges (R-S boundary) split more and these tilted edges grow laterally as the overall size of the particle increases (stage II). As the chiral components of the tilted edges developed, the g -factor increased rapidly.

In the case of 432 helicoid II, the evolution direction of the chiral components is completely different. For the initial 30 min (stage I), the AB and A'B' edges of the rhombus ABA'B' expand with distortion. The distortion takes place gradually as a result of the increase in the R region. Distinctive edge growth was observed only after 40 min (stage II). During stage II, as the distorted edges became thicker, the chiral components were more distinguishable, increasing the g -factor. According to the quantification result (Extended Data Fig. 4e), the amount of adsorbed GSH also increased at this growth stage. The increasing trend of adsorbed peptides with growth time is similar to that of g -factor (Extended Data Fig. 4d). This finding implies that the evolution of chirality is closely related to the adsorption of GSH on the gold surface. Furthermore, different increasing trends in the g -factor between 432 helicoids I and II indicate that contrasting binding kinetics between Cys and GSH on the gold surface.

Numerical calculations. We analysed the optical activity of the chiral nanoparticles using a three-dimensional full-wave numerical simulation using a commercial-grade simulator (Lumerical). The calculations were based on the finite-difference time-domain (FDTD) method. The geometry of the simulation model was deduced from SEM images and a mesh was constructed non-uniformly, with a mesh size of less than 10 nm near the nanoparticles. The refractive index of water was assigned a value of 1.33 and the optical properties of gold were taken from a previous study⁴⁰.

The FDTD simulation calculates the scattering (C_{sca}) and absorption (C_{abs}) cross-sections of a given particle. The extinction cross-section ($C_{\text{ext}} = C_{\text{abs}} + C_{\text{sca}}$) is used to estimate the macroscopic absorption. According to the Beer-Lambert law, the transmission T and absorbance A through a medium of thickness l and filled with particles to a number density N is represented by $T = I/I_0 = \exp(-NIC_{\text{ext}})$ and $A = -\log_{10}(T)$. A chiral-particle medium exhibits different absorbance to left (LCP) and right (RCP) circularly polarized light (A_{L} and A_{R}); the CD calculated from this absorbance difference is approximated as

$$\text{CD} \approx (A_{\text{L}} - A_{\text{R}}) \frac{\log(10)}{4} \text{rad} = (A_{\text{L}} - A_{\text{R}}) \frac{\log(10)}{4} \frac{180}{\pi} \text{deg}$$

Here, the orientation average over 756 directions was used to account for the random orientation of the chiral nanoparticles in a water medium. The incident illumination of an electromagnetic wave travels in the $+z$ direction. Under this fixed-illumination condition, nanoparticles were rotated in three-dimensions;

the polar angle (Θ) was changed from 0° to 180° and the azimuthal angle (Φ) was simultaneously changed from 0° to 360° (Extended Data Fig. 7d). Therefore, the orientation-averaged extinction ($\langle C_{\text{ext}} \rangle_{\Omega}$) and CD ($\langle \text{CD} \rangle_{\Omega}$) could be calculated.

The electromagnetic field near the plasmonic helicoid was calculated at a normal incidence ($\Theta = 0^\circ$ and $\Phi = 0^\circ$) with a uniform mesh size of 2 nm. The electric- and magnetic-field distributions on the illuminated surface were displayed at selected wavelengths (650 nm, 950 nm and 1,200 nm); the field differences, $(|E_{\text{LCP}}|^2 - |E_{\text{RCP}}|^2)/E_0^2$ and $(|B_{\text{LCP}}|^2 - |B_{\text{RCP}}|^2)/B_0^2$, are representative of the microscopic asymmetric responses, where E_0 (B_0) indicates an amplitude of the initial electric (magnetic) field. We analysed the multipolar contribution to scattering through multipole decomposition from the calculated electromagnetic-field vectors⁴¹.

Design guidelines of chiral nanoparticles. Efforts to quantify chirality and to correlate geometric chirality with the observed chiral property have encountered many difficulties in many disciplines⁴². Despite the difficulty in correlating structural chirality with the observed macroscopic chiral properties, we tried to obtain general design guidelines for achieving large chiral responses by restricting ourselves to certain chiral particle designs (Extended Data Fig. 8). Although there are no universal design principles to intuitively predict the relationship between structural chirality and the optical chiral response, we obtained chiral responses for fixed structure designs of chiral nanoparticles using computational electrostatics, which can be used to successfully express the optical properties of nanoparticles; that is, we can predict the morphologies of nanoparticles that will exhibit better performance. However, it is impossible to study any arbitrary design using computationally intensive full-wave numerical simulations; therefore, we show only some design guidelines for chiral nanoparticles using simplified models from SEM images (Fig. 3a, b), retaining the characteristic four-fold rotational symmetry of the helicoids.

To estimate the chiral properties of chiral nanoparticles, we first calculated the scattering cross-section and absorption cross-section of a single chiral nanoparticle at LCP and RCP incidences using FDTD with a total-field scattered-field formalism and perfectly matched layer (PML) absorbing boundaries in a water medium ($n = 1.33$). We considered random orientations of the colloidal chiral nanoparticles by rotating them to discrete orientations and averaging the results. Because the simulation of many particles with different orientations is time consuming, we simulated using a uniform 4-nm mesh. However, for some chiral nanoparticles with small feature sizes (< 20 nm), a 3-nm mesh was used. We checked some of the results against those calculated with a 1-nm mesh and found no substantial differences, although the responses obtained with a 1-nm mesh were slightly stronger.

Absorbance (abs), CD and g -factor are characterized as follows:

$$\begin{aligned} \text{abs} &= \frac{NI \sum C}{2 \log(10)} \\ \text{CD} &= \frac{NI \Delta C}{4} \\ g\text{-factor} &= 2 \frac{\Delta C}{\sum C} \end{aligned}$$

where $\sum C \equiv \langle C_{\text{ext,LCP}} \rangle_{\Omega} + \langle C_{\text{ext,RCP}} \rangle_{\Omega}$, $\Delta C \equiv \langle C_{\text{ext,LCP}} \rangle_{\Omega} - \langle C_{\text{ext,RCP}} \rangle_{\Omega}$; $\langle \dots \rangle_{\Omega}$ represents an average over all orientations, $N = 1 \times 10^{15} \text{ m}^{-3}$ is the particle number density, and $l = 1 \times 10^{-3} \text{ m}$ is the optical path length. With this definition, the g -factor is constrained between -2 and 2 .

It is well known that larger particles can support stronger dipole moments and higher-order modes, which can lead to stronger extinction and chiral responses. Extended Data Fig. 8a supports this claim, with chiral nanoparticles (samples 1–3) with increasing edge lengths (size of particle) in the same geometry showing increasing g -factors. However, to function as a metamaterial, the meta-atom, or chiral nanoparticle, should be smaller than the wavelength of the incident light; hence, the size of the chiral nanoparticle is limited to some extent. Remarkably, the optical properties of the chiral nanoparticles (both extinction and chirality) depend strongly on their subwavelength plasmonic gap. Generally, chiral nanoparticles with narrower and deeper plasmonic gaps exhibit a stronger and redshifted extinction and chiral response. The results are summarized in Extended Data Fig. 8a, in which chiral nanoparticles (samples 4–7) with increasing gap widths have decreasing g -factors and those (samples 8–14) with increasing gap depths have increasing g -factors of more than 0.7. These stronger and redshifted features may originate from a stronger dimeric coupling between the two domains separated by the plasmonic gap. This could be explained by the plasmon-hybridization model, which explains the behaviour of closely coupled plasmonic nanostructures due to the electrostatic dipole-dipole interaction resulting in an enhanced and stabilized (redshifted in wavelength) response⁴³. We also found an enhanced electric field near the plasmonic gaps in Extended Data Fig. 8b, which can result in enhanced dipole moments. This field enhancement increased as the plasmonic gap became

narrower and deeper. We also studied chiral nanoparticles (samples 16–19) with different gap angles, which is essential for the broken parity symmetry and chiral response. An achiral nanoparticle with a gap angle of 0° or 90° will not exhibit any chiral response; however, it is still difficult to quantify the structural chirality of the other chiral nanoparticles studied here.

We also simulated chiral nanoparticles with more complex geometries (Extended Data Fig. 8c). The difficulty in correlating structural chirality to the observed chiral properties is also addressed by the decreasing g -factor of chiral nanoparticles with increases in certain curvatures in samples 20–22. As stated above, structural chirality cannot be quantified and we generally rely on numerical methods or experiments to predict chiral properties. In samples 23–26, the extinction of elongated chiral nanoparticles showed noticeable changes due to an increase in size, but their g -factors remained similar despite large changes in their aspect ratio and size, of up to a factor of three. The four-fold symmetry of our chiral nanoparticle gets broken, and the orientation dependence of responses becomes larger. In sample 32, the triangular plate also showed noticeable orientation-dependent responses. This anisotropic response has commonly been observed in canonical chiral systems, such as helices, twisted-nanorods and helical arrangements of nanoparticles, and is responsible for the lowering of the average chiral response. In samples 27–31, different chiral particle designs, such as hollow chiral nanoparticles, were constructed by removing cubic domains inside the chiral nanoparticle. In samples 27 and 28, which have small void sizes, the particles did not exhibit noticeable change in their responses. However, chiral nanoparticles with large voids (samples 29–31) had g -factors of more than 0.9—the strongest g -factor of these simulations. These hollow chiral nanoparticles have very thin outer shells and exposed insides. Interestingly, strongly enhanced and redshifted responses were observed despite the greatly reduced volume.

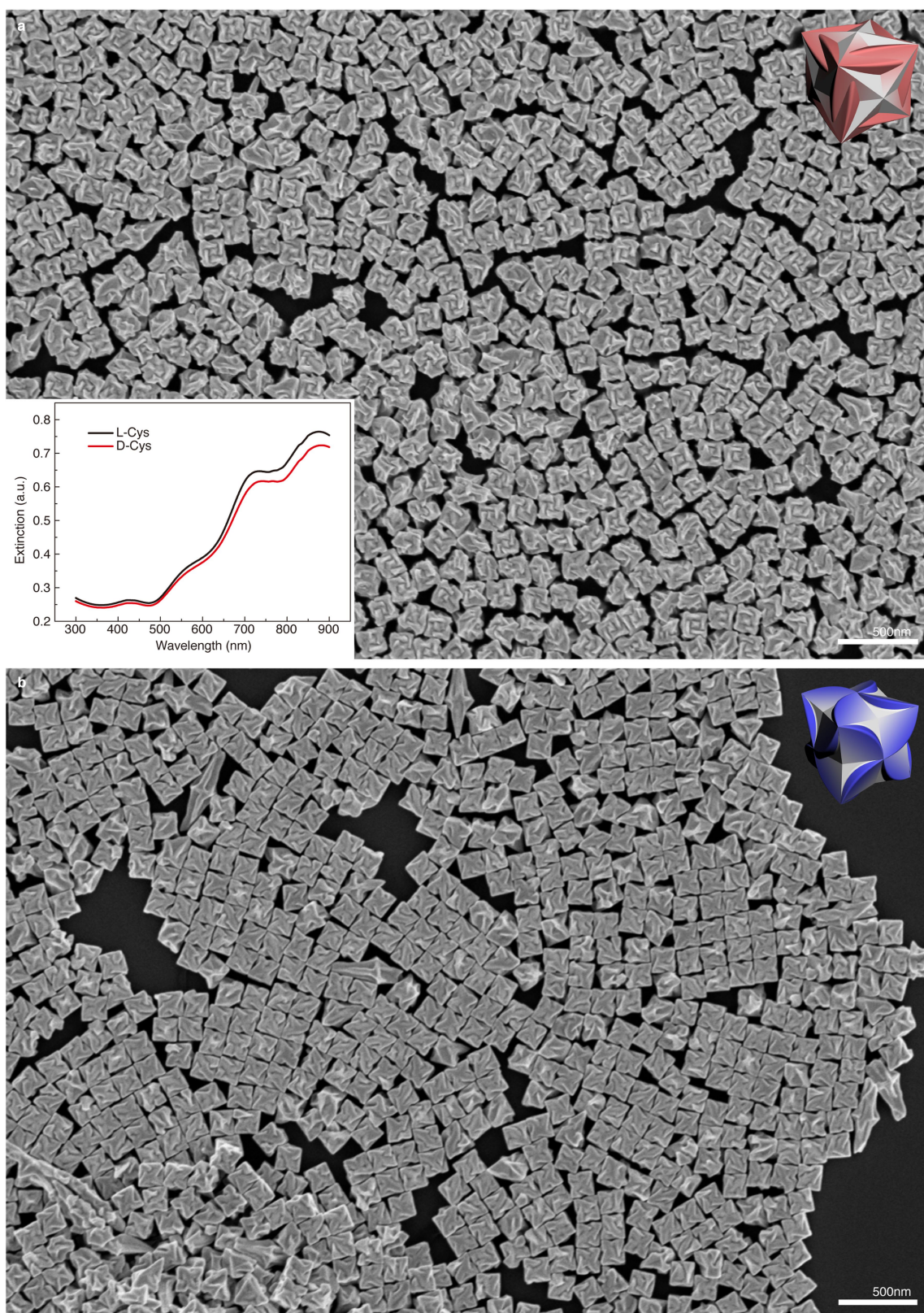
The properties of small chiral particles or chiral molecules are often explained using electric and magnetic dipole moments. This description is consistent for small chiral systems with spectrally overlapping absorption and chiral responses, which essentially limit the available g -factor. Interestingly, we observed enhanced g -factors along with enhanced CD despite increasing extinction and CD. This is because their peaks do not appear at the same wavelength and the CD peak appears between the fundamental and higher-order modes of extinction. This separation of the extinction modes appears with the redshifted response and may arise from higher-order plasmon modes. The excitation of higher-order modes using plasmon hybridization has often been reported in the field of plasmonic metamaterials⁴³ and could have a role in our chiral nanoparticles, in which nanogaps much smaller than the wavelength effectively change the overall response.

In summary, we have developed some general guidelines for designing chiral nanoparticles with high g -factors. First, both the extinction (absorbance) and chiro-optical response (CD, g -factor) depend on the size of chiral nanoparticles. This is because a larger particle supports stronger dipolar modes and even higher-order modes, resulting in stronger extinction and chiro-optical responses. Second, in general, the chiro-optical properties of chiral nanoparticles depend strongly on their 'gap'. Although the feature size of these gaps is much smaller than the wavelength, plasmonics allows considerable changes in response with subtle morphology differences. Narrower and deeper gaps allow stronger and redshifted chiro-optical responses as well as extinction, which could originate from stronger dimeric

plasmon coupling. The high-performance plasmonic chiral systems reported so far often have discrete particles that are coupled to achieve the enhanced responses. These chiral systems have linker molecules, such as DNA, to maintain their conformations. A single continuous chiral nanoparticle could have a similar property owing to the gaps that are deep and long. Therefore, designing chiral nanoparticles with high performance requires control over gap formation. Third, hollow chiral nanoparticles could achieve highly enhanced chiro-optical properties with g -factor of 0.9. In addition, the redshifted response without an increase in particle size could be beneficial because it decreases the particle-size-to-wavelength ratio, which brings this particle medium closer to the definition of a metamaterial.

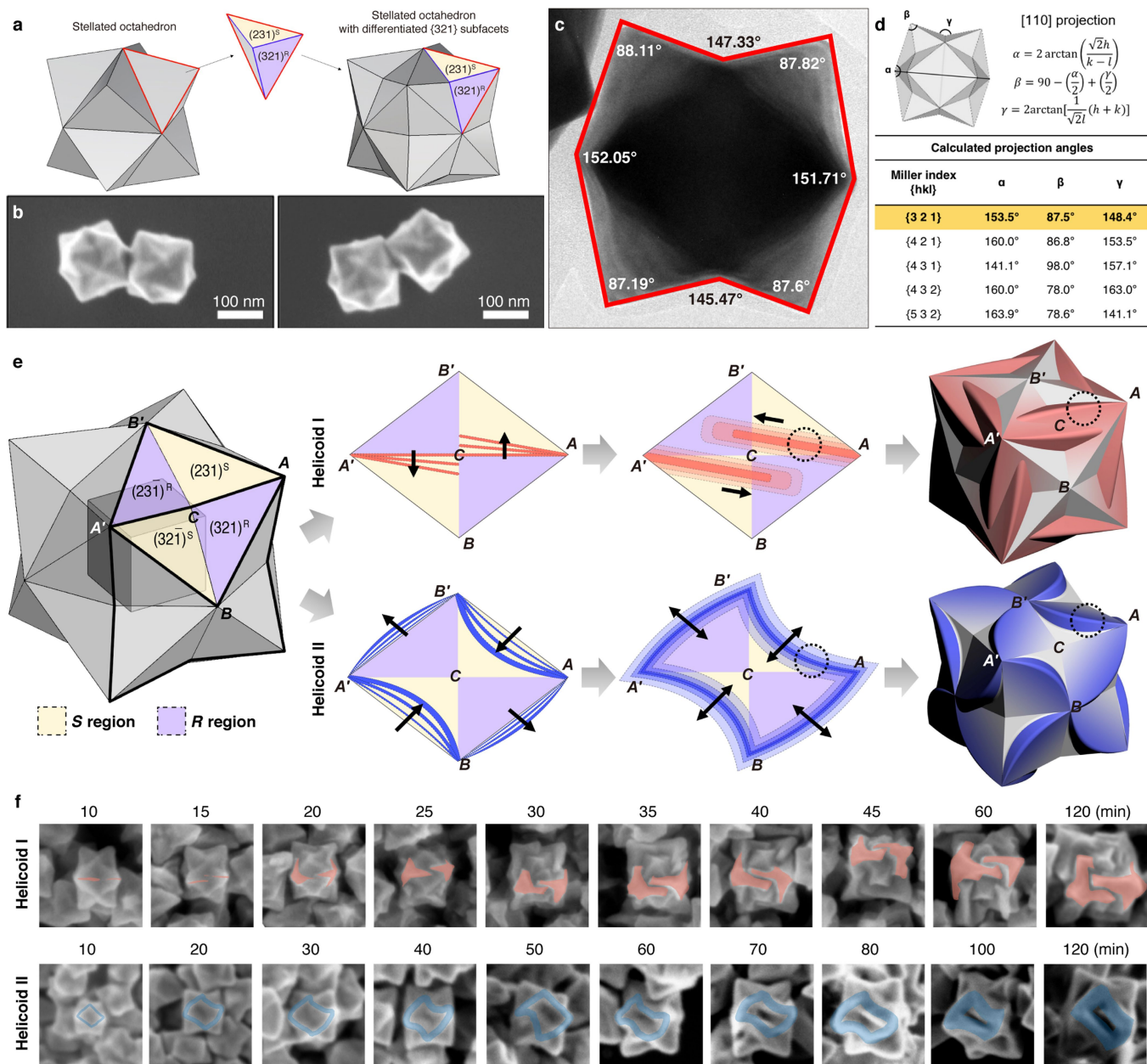
Data availability. The data that support the findings of this study are available from the corresponding authors on reasonable request.

34. Wu, H. L. et al. A comparative study of gold nanocubes, octahedra, and rhombic dodecahedra as highly sensitive SERS substrates. *Inorg. Chem.* **50**, 8106–8111 (2011).
35. Ansar, S. M. et al. Removal of molecular adsorbates on gold nanoparticles using sodium borohydride in water. *Nano Lett.* **13**, 1226–1229 (2013).
36. Yuan, M. et al. A method for removing self-assembled monolayers on gold. *Langmuir* **24**, 8707–8710 (2008).
37. Arrigan, D. W. M. & Bihan, L. L. A study of L-cysteine adsorption on gold via electrochemical desorption and copper(II) ion complexation. *Analyst* **124**, 1645–1649 (1999).
38. Bieri, M. & Bürgi, T. Adsorption kinetics of L-glutathione on gold and structural changes during self-assembly: an in situ ATR-IR and QCM study. *Phys. Chem. Chem. Phys.* **8**, 513–520 (2006).
39. Bieri, M. & Bürgi, T. L-glutathione chemisorption on gold and acid/base induced structural changes: a PM-IRRAS and time-resolved in situ ATR-IR spectroscopic study. *Langmuir* **21**, 1354–1363 (2005).
40. Johnson, P. B. & Christy, R. W. Optical constants of the noble metals. *Phys. Rev. B* **6**, 4370–4379 (1972).
41. Grahm, P., Shevchenko, A. & Kaivola, M. Electromagnetic multipole theory for optical nanomaterials. *New J. Phys.* **14**, 093033 (2012).
42. Barron, L. D. Chemistry: Compliments from Lord Kelvin. *Nature* **446**, 505–506 (2007).
43. Prodan, E., Radloff, C., Halas, N. J. & Nordlander, P. A hybridization model for the plasmon response of complex nanostructures. *Science* **302**, 419–422 (2003).
44. McPhie, P. Circular dichroism studies on proteins in films and in solution: estimation of secondary structure by g -factor analysis. *Anal. Biochem.* **293**, 109–119 (2001).
45. Maoz, B. M. et al. Plasmonic chiroptical response of silver nanoparticles interacting with chiral supramolecular assemblies. *J. Am. Chem. Soc.* **134**, 17807–17813 (2012).
46. Hao, C. et al. Unusual circularly polarized photocatalytic activity in nanogapped gold-silver chiroplasmonic nanostructures. *Adv. Funct. Mater.* **25**, 5816–5822 (2015).
47. Wu, X. et al. Unexpected chirality of nanoparticle dimers and ultrasensitive chiroplasmonic bioanalysis. *J. Am. Chem. Soc.* **135**, 18629–18636 (2013).
48. Yan, W. et al. Self-assembly of chiral nanoparticle pyramids with strong R/S optical activity. *J. Am. Chem. Soc.* **134**, 15114–15121 (2012).
49. Lan, X. et al. Au nanorod helical superstructures with designed chirality. *J. Am. Chem. Soc.* **137**, 457–462 (2015).
50. Yan, J., Hou, S., Ji, Y. & Wu, X. Heat-enhanced symmetry breaking in dynamic gold nanorod oligomers: the importance of interface control. *Nanoscale* **8**, 10030–10034 (2016).



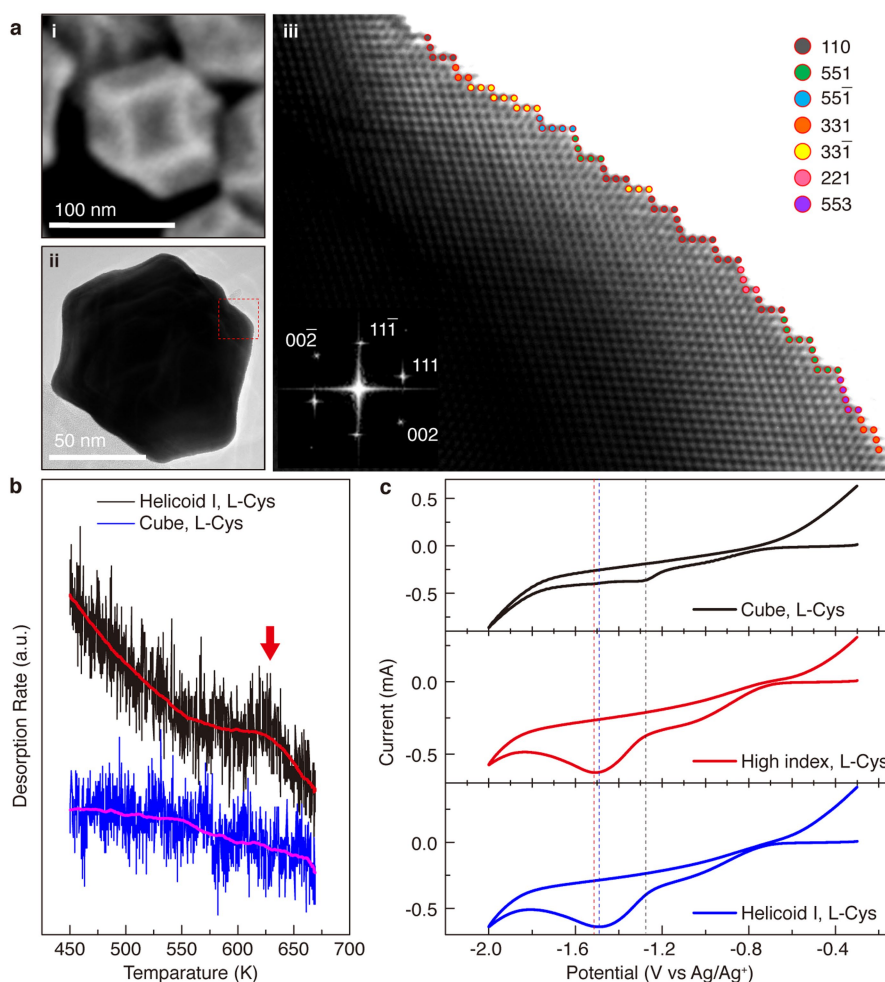
Extended Data Fig. 1 | Chiral morphology and characterization of 432 helicoids I and II. a, Large-area SEM image of 432 helicoid I. L-Cys was used as an additive. Inset, extinction spectra of 432 helicoid I synthesized

using L-Cys and D-Cys. **b,** Large-area SEM image of 432 helicoid II, synthesized with L-GSH.



Extended Data Fig. 2 | Chiral morphology development of 432 helicoids I and II. **a**, Schematic illustration of stellated octahedron with differentiated $\{321\}$ facets ($\{321\}$ nanoparticle). Each triangular facet of a stellated octahedron is divided into two convex $\{321\}$ facets with *R* and *S* surface conformation. **b**, SEM images showing the detailed geometry of a $\{321\}$ nanoparticle. **c**, Bright-field TEM image along the $[110]$ direction showing angles (α, β, γ) between the eight outermost edges. **d**, Calculated angles between the outermost edges of an $\{hkl\}$ -enclosed nanoparticle.

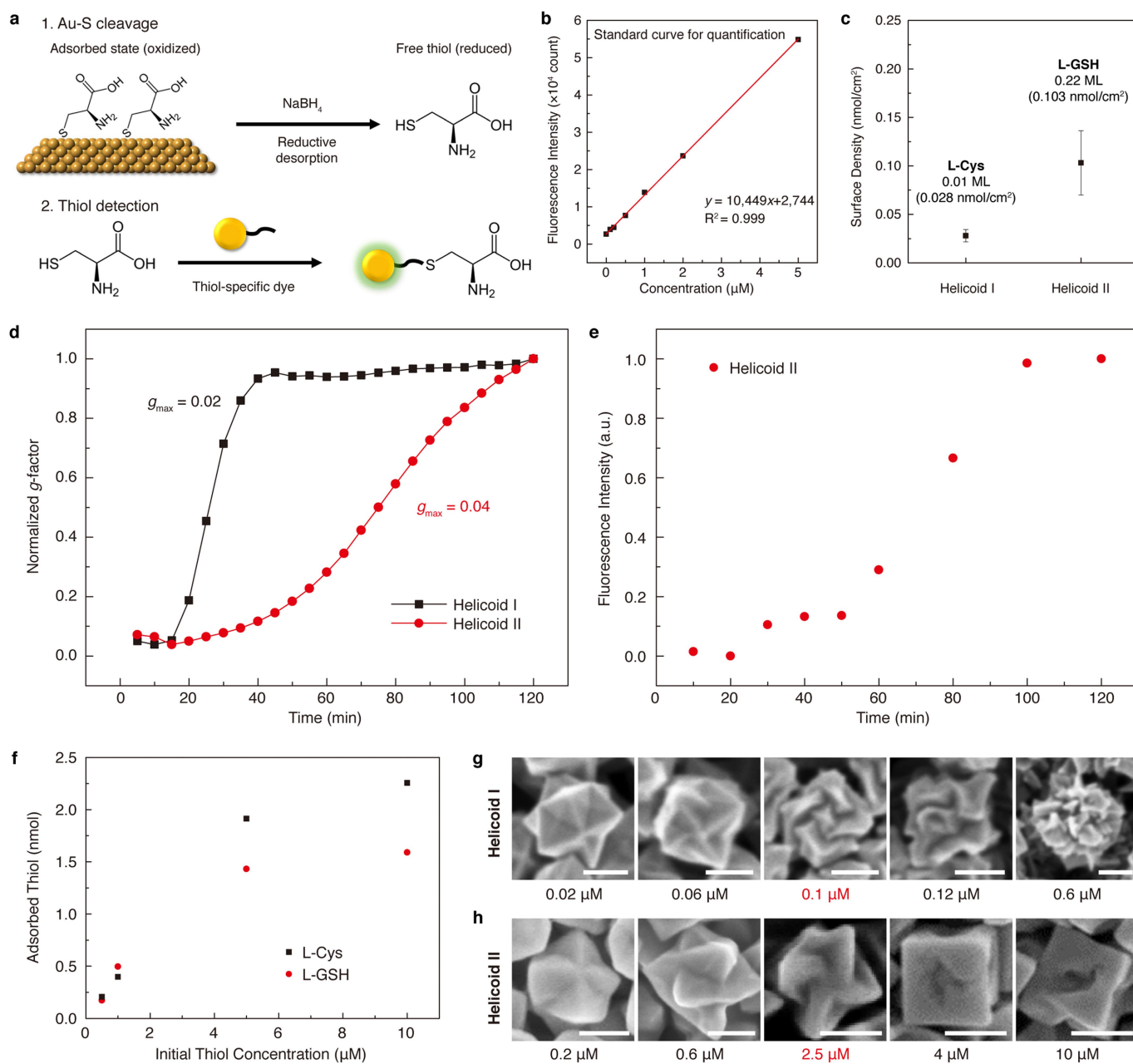
The exposed facets of the nanoparticle in **c** were indexed as $\{321\}$. **e**, Schematic illustration of the time-dependent evolution of 432 helicoids I and II. All models are viewed along the $[110]$ direction. Starting from a $\{321\}$ -indexed nanoparticle with an equal ratio of *R* and *S* regions, different *R*-*S* boundaries are split, thickened and distorted. **f**, SEM images of 432 helicoids I and II at different growth times. The chiral components that developed in 432 helicoids I and II are highlighted in red and blue, respectively.



Extended Data Fig. 3 | Interaction of L-Cys with high-index planes.

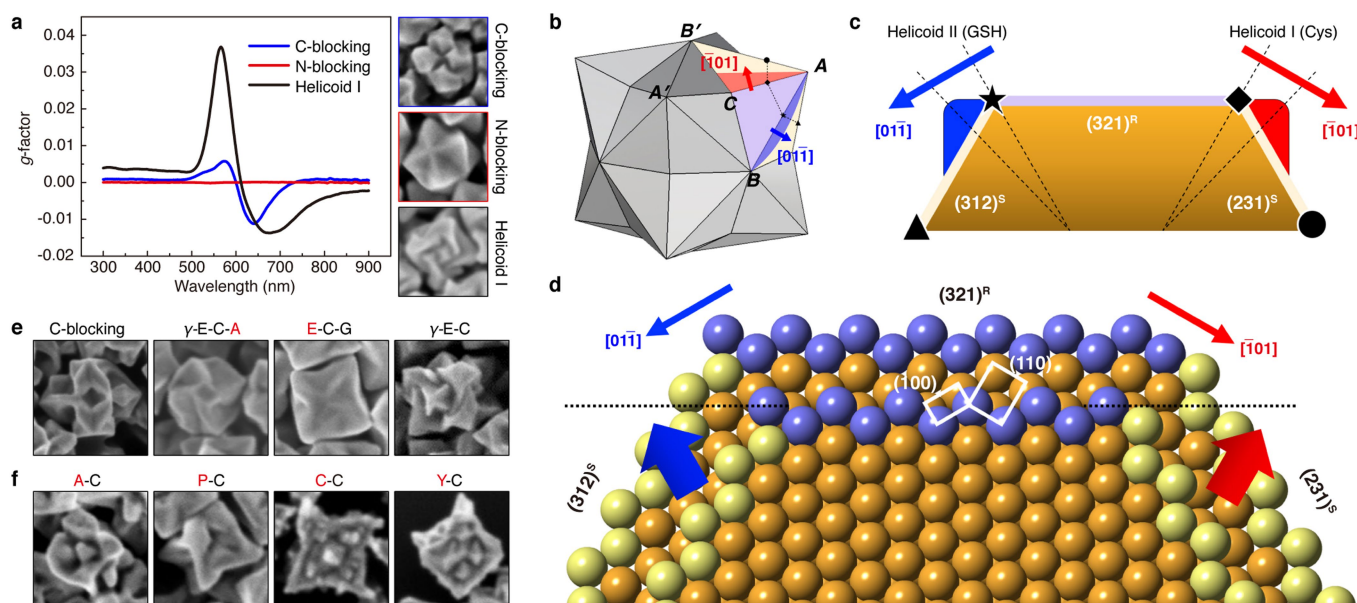
a, Atomic structure of a chiral nanoparticle at the initial stage. SEM image (i) and TEM images (ii and iii) of a chiral nanoparticle after 20 min of growth. Because the nanoparticle was oriented along the $\langle 110 \rangle$ direction, the projected boundaries in the TEM image consist of chirally distorted edges. The high-resolution TEM image of distorted edges corresponds to the red dotted box in ii. The atoms of the microfacets are marked with coloured circles, and different colours are assigned to the Miller index of each microfacet. Using microfacet nomenclature, the microstructure of (551) can be divided into three units of (111) and two units of ($11\bar{1}$). Inset, corresponding fast Fourier transform (FFT) showing typical patterns along the $[1\bar{1}0]$ zone. **b**, Temperature-programmed desorption spectra of L-Cys of 432 helicoid I and a low-index cubic nanoparticle, with

monitoring of CO_2 ($m/q = 44 \text{ AMU}$). As the temperature was raised at a rate of 3 K min^{-1} , helium carrier gas flowed over the dried nanoparticle sample. The distinguishable temperature-programmed desorption peak at 635 K for 432 helicoid I indicates a specific interaction of L-Cys with a kink atom on the gold surface. Cys on the cube (100) surface shows no observable peak at high temperatures. **c**, Cyclic voltammograms for a cube, a high-index stellated octahedron (with differentiated $\{321\}$ facets) and 432 helicoid I, with L-Cys measured in 0.1 M KOH-ethanol solution at a scan rate of 0.1 V s^{-1} . Negative peaks between about -1.8 V and -1.1 V originate from the reductive desorption of L-Cys by the cleavage of an Au-S bond, $\text{Au-SR} + e^- \rightarrow \text{Au} + \text{RS}^-$. Desorption peaks at more negative potentials indicate the higher adsorption energy of L-Cys on high-index gold surfaces.



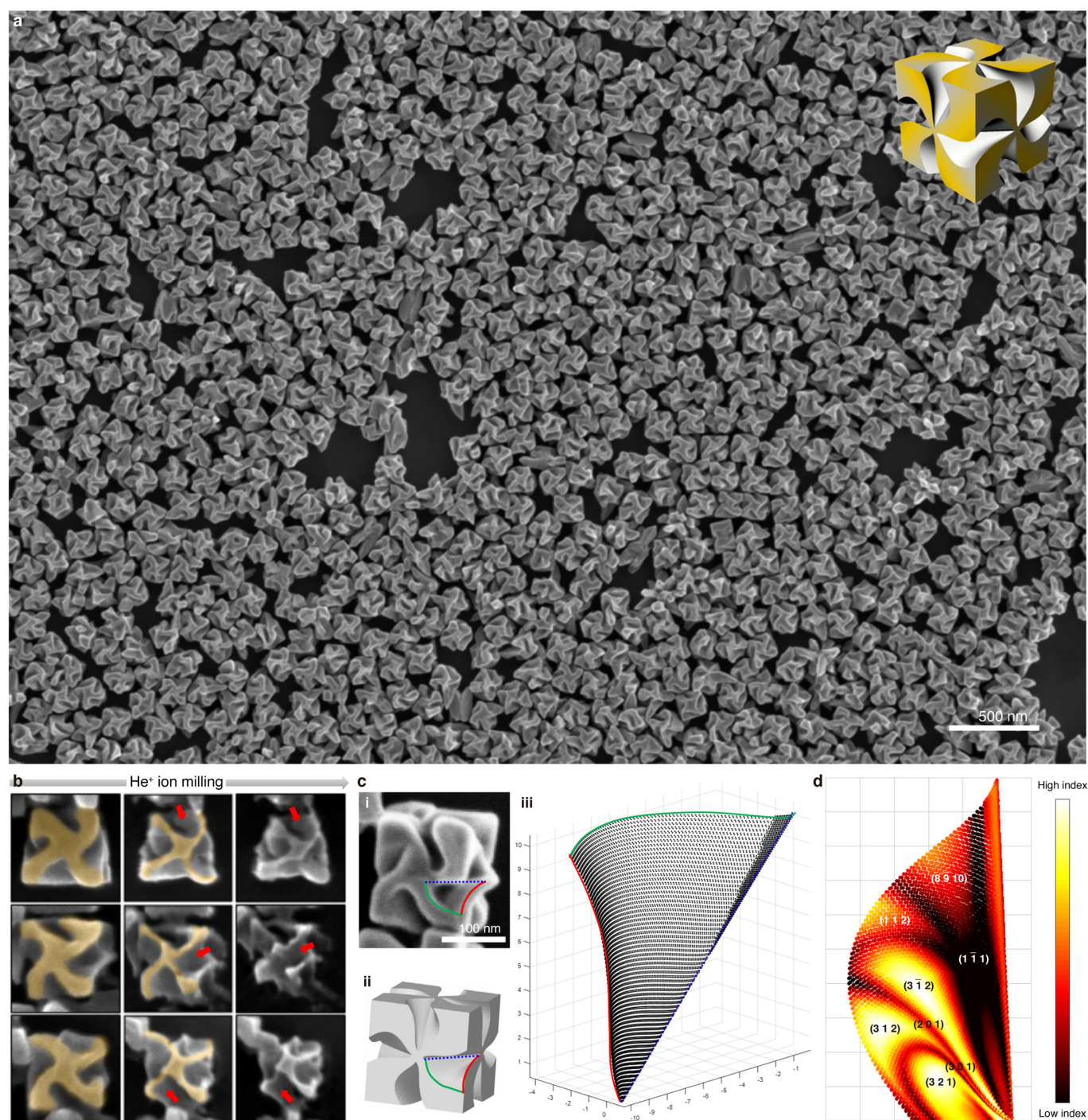
Extended Data Fig. 4 | Comparison of Cys and GSH by time-dependent concentration quantification and adsorption assay. **a**, Schematic experimental procedure for thiol quantification on the gold surface. The reduction of thiolate by NaBH_4 cleaved the Au-S bond, and the thiol group of the released molecule spontaneously reacted with the thiol-specific dye, producing a fluorescent derivative. The excitation and emission wavelengths were 405 nm and 535 nm, respectively. **b**, Concentration curve from 0 μM to 5 μM for a fluorometric assay of L-Cys. The linear fitting and corresponding R^2 value show good linearity within the measured range. **c**, Measured surface density of L-Cys and L-GSH for 432 helicoids I and II, respectively. Surface coverage is calculated using the previously reported surface densities of L-Cys and L-GSH at the fully saturated monolayer condition. Mean \pm s.d. ($n = 3$) is shown. **d**, Increase in g -factor of 432 helicoids I (Cys) and II (GSH) with time. The CD signal was measured and the normalized g -factor is displayed every 5 min during growth. The maximum g -factors (g_{max}) of 432 helicoids I and II at 120 min were

0.02 and 0.04, respectively. **e**, Amount of GSH adsorbed on 432 helicoid II at different growth times. For a detailed quantification of the amount of GSH on a nanoparticle, see Methods. **f**, Adsorption study of Cys and GSH on {321} nanoparticles. Different concentrations of Cys and GSH were added and aged for 2 h, and the amount of adsorbate was measured by subtracting the Cys and GSH concentrations in the supernatant from the initial concentration. See Methods for a detailed Cys and GSH quantification study. **g**, **h**, Effect of Cys and GSH concentrations on chiral morphology. SEM images of chiral nanoparticles synthesized with different concentrations of Cys (**g**) and GSH (**h**). The highest g -factor was observed at the optimum amino acid and peptide concentration (red text). At low concentrations, only achiral nanoparticles formed, but with incremental additions, chiral edges started to appear. An excess of molecule results in the overgrowth of edges and a greatly decreased CD signal, indicating that an optimal concentration exists for chirality formation. Scale bars, 100 nm.



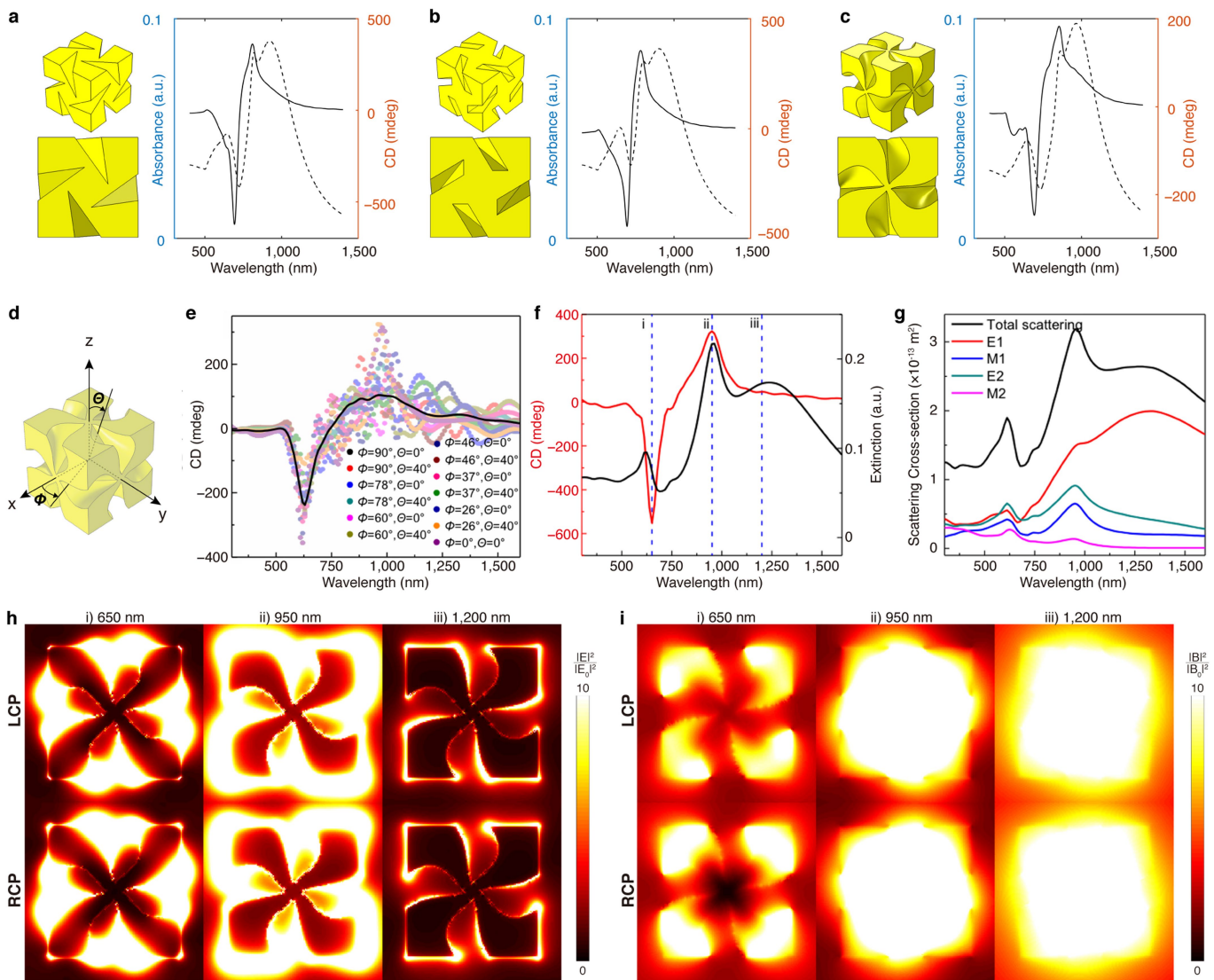
Extended Data Fig. 5 | Effect of molecular structure on chirality evolution. **a**, Effect of functional-group change in L-Cys. Comparison of g -factor and SEM images of synthesized nanoparticles with C-terminal blocked L-Cys (L-cysteine ethyl ester) (top), N-terminal blocked L-Cys (N-acetyl-L-cysteine) (middle) and L-Cys (bottom). C-blocked L-Cys changed the chiral morphology and decreased the CD intensity of the resulting nanoparticles. Furthermore, nanoparticles produced with N-blocked L-Cys showed achiral morphology without an observable CD signal. **b**, Schematic illustration of chirality formation on a $\{321\}$ nanoparticle. Boundary shifts of 432 helicoids I (L-Cys) and II (L-GSH) are indicated in red and blue, respectively. **c**, Schematic (111) cross-section of $(312)^S$ – $(321)^R$ – $(231)^S$ facets. Original and newly shifted R–S boundaries are indicated with dashed lines. **d**, Atomic arrangement of

$(312)^S$ – $(321)^R$ – $(231)^S$ facets in a (111) cross-section view. The $\{321\}$ surface consists of a (111) terrace and alternating $\{100\}$ and $\{110\}$ microfacets. The \overline{AC} boundary in 432 helicoid I shifts in the $[\overline{1}01]$ direction and the \overline{AB} boundary in 432 helicoid II shifts in the $[01\overline{1}]$ direction. The differentiated growth directions at $(312)^S$ and $(231)^S$, indicated with thick arrows, resulted in contrasting morphology for the different chiral nanoparticles. **e**, Effect of functional-group change in L-GSH. SEM images are shown of the synthesized nanoparticles prepared with L-glutathione ethyl ester (C-blocking), γ -E-C-A, E-C-G and γ -E-C sequences. **f**, SEM images of nanoparticles synthesized with different dipeptide sequences. Alanine (A), proline (P), cysteine (C) or tyrosine (Y) was added to the N terminus of L-Cys, which modified the morphology of the resulting nanoparticle substantially.



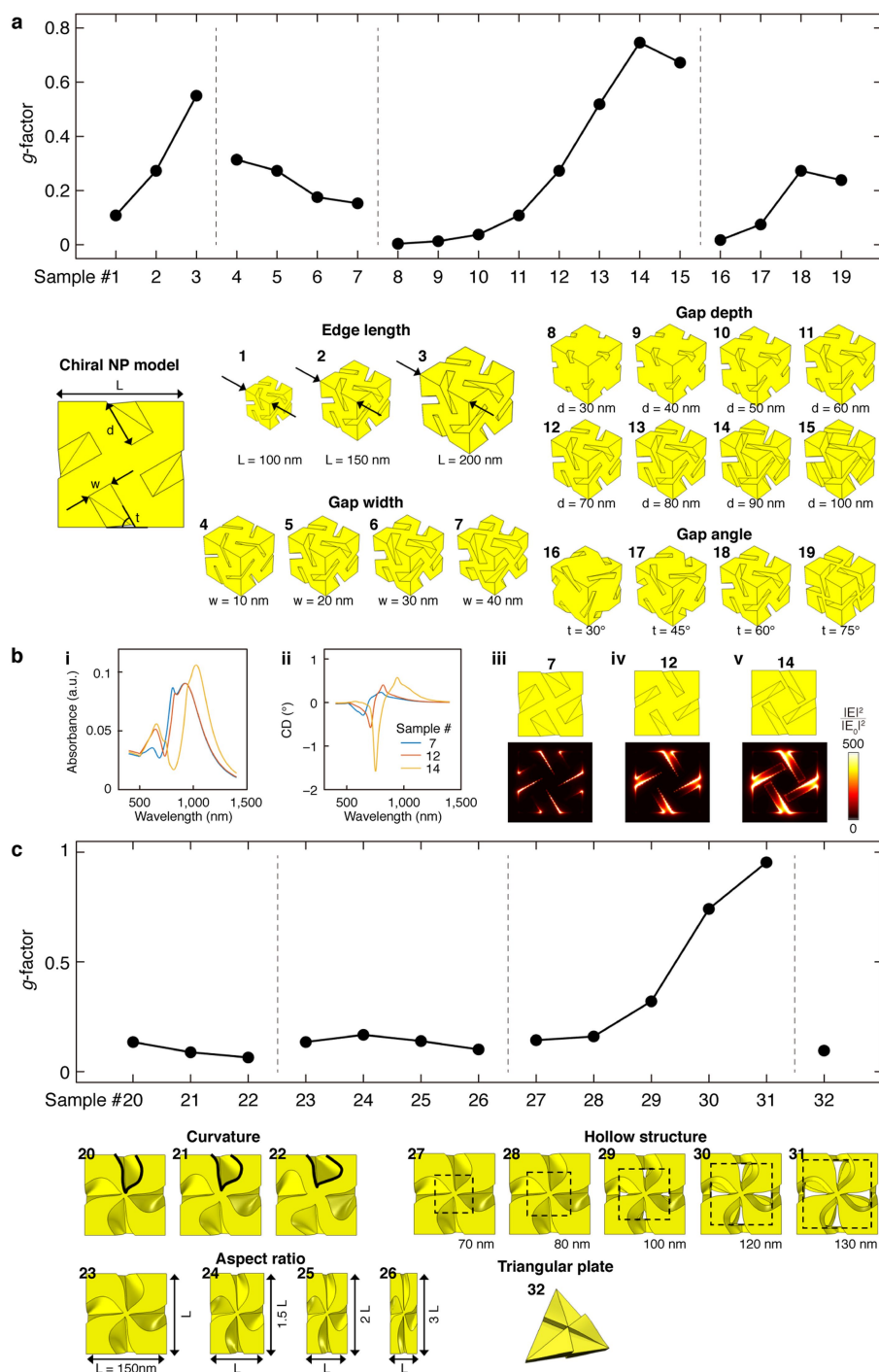
Extended Data Fig. 6 | Characterization of surfaces inside the gaps of 432 helicoid III. **a**, Large-area SEM image of 432 helicoid III nanoparticles, synthesized using an octahedral seed and L-GSH. **b**, Helium-ion microscopy secondary electron images of 432 helicoid III during the He⁺-ion milling process. The original pinwheel-like structure of 432 helicoid III is highlighted in yellow. Exposure to a He⁺-ion beam with an acceleration voltage of 30 keV and a beam current of 0.733 pA allows visualization of the interior parts of the curved surfaces, as indicated by red arrows. **c**, Modelling of the 432 helicoid III surface.

A magnified SEM image of 432 helicoid III (i), the corresponding three-dimensional model (ii) and the interpolated curved surface of 432 helicoid III (iii) are shown. The curved outlines of the chiral arm at the front and side face are indicated by green and red lines, respectively, and the internal boundary is indicated by the blue dotted lines. The three-dimensional curved-surface model of 432 helicoid III was constructed by using the interpolation of surface outlines. **d**, Distribution of Miller indices on the modelled surface. The Miller indices were calculated from a normal vector at each point on the surface.



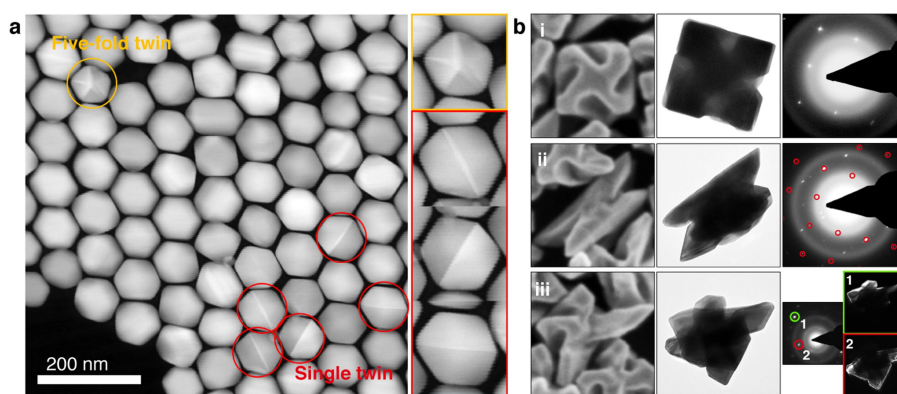
Extended Data Fig. 7 | FDTD simulation results for 432 helicoid III. **a–c**, Calculated absorbance (dashed lines) and CD (solid lines) for 432 helicoid III with triangular (**a**), rectangular (**b**) and curved (**c**) gap shapes. The corresponding three-dimensional models are displayed on the left. All three models derived from SEM images of the particles successfully reproduce the experimentally observed characteristic spectrum patterns: two main absorbance peaks, a sharp absorbance feature overlapped on the fundamental absorbance peak, a CD peak overlapped on the sharp feature, and the ‘bisignate’ CD signals, with negative peaks near 700 nm and a positive peak around 800–850 nm. This reproduction of the general features of 432 helicoid III suggests that the models can be used to study this helicoid theoretically and that they do not have to be perfect, but only need to resemble the helicoid shape sufficiently. All of the results are averaged over 756 discrete orientations and were estimated using a particle number density of $N = 10^{15} \text{ m}^{-3}$ and a cell path

length of $l = 10^{-3} \text{ m}$. **d**, Three-dimensional model and orientation of 432 helicoid III. **e**, Orientation-averaged CD spectrum ($\langle \text{CD} \rangle_{\Omega}$, black solid line) and CD spectra calculated at selected orientations (dots). $\langle \text{CD} \rangle_{\Omega}$ is averaged over 756 discrete orientations. The CD spectrum at a single orientation resembles $\langle \text{CD} \rangle_{\Omega}$ with some deviations. **f**, CD and absorbance spectra calculated with a normal incidence. **g**, Scattering cross-section decomposed by multipole analysis. The total scattering is contributed by a broad and large electric dipole mode (E1) around 1,200 nm, and a magnetic dipole (M1) and electric quadrupole (E2) around 650 nm and 950 nm near the chiro-optical peaks. A strong chiro-optical signal was observed from two other high-order modes (650 nm and 950 nm). **h, i**, Electric- and magnetic-field intensities on an illuminated helicoid surface upon normal incidence of LCP and RCP light at three different wavelengths (650 nm, 950 nm and 1,200 nm).



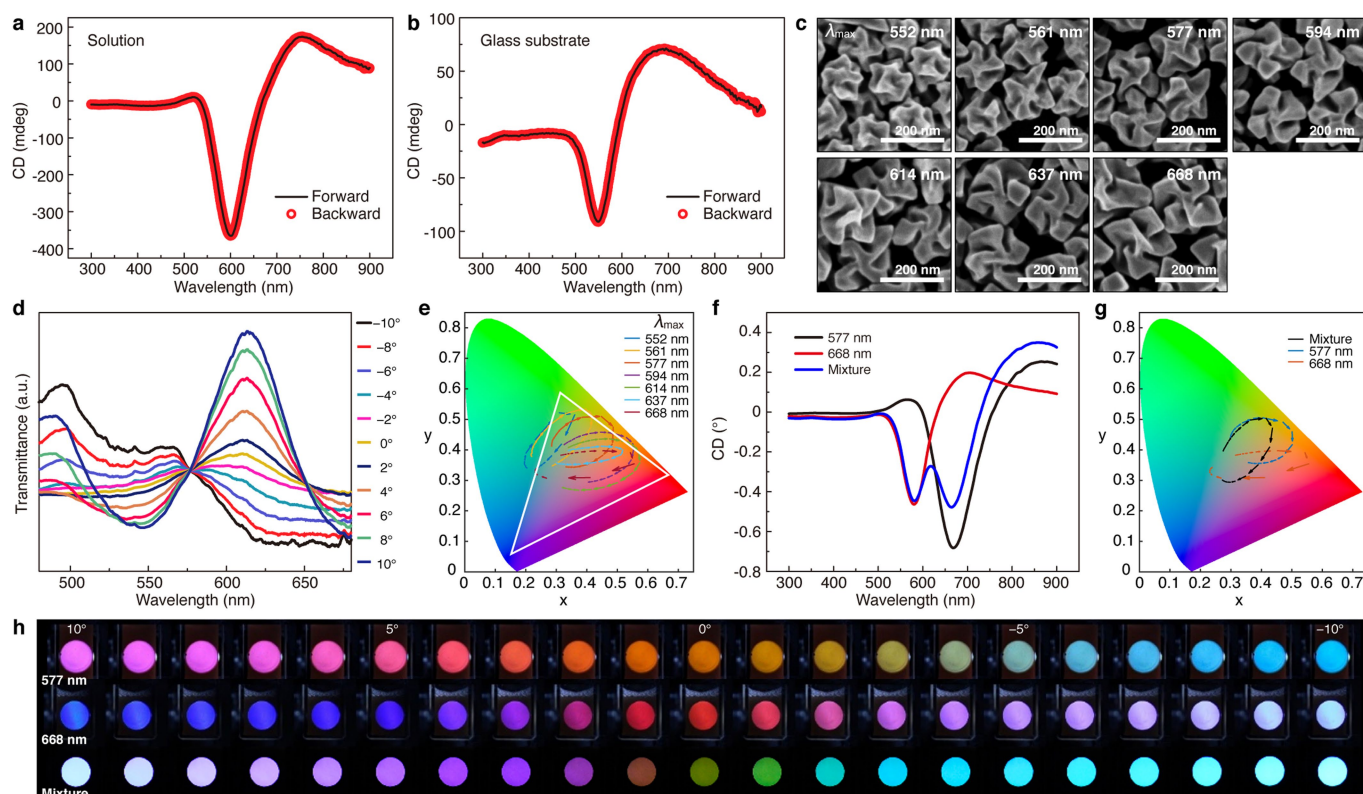
Extended Data Fig. 8 | FDTD simulations of differently modified 432 helicoid III nanoparticles to identify design guidelines. a, Calculated g -factors of chiral nanoparticles corresponding to models using parameterized chiral nanoparticles (samples 1–19). The different samples represent chiral nanoparticles with: 1–3, edge lengths L of 100–200 nm; 4–7, gap widths w of 10–40 nm; 8–15, gap depths d of 30–100 nm; or 16–19, gap angles t of 30° – 75° . The default parameters are $L = 150$ nm, $w = 20$ nm, $d = 70$ nm and $t = 60^\circ$. **b,** Calculated absorbance and CD of chiral nanoparticle samples 7 ($L = 150$ nm, $w = 40$ nm, $d = 70$ nm, $t = 60^\circ$), 12 ($L = 150$, $w = 20$, $d = 70$, $t = 60$) and 14 ($L = 150$, $w = 20$, $d = 90$, $t = 60$), using $N = 10^{15} \text{ m}^{-3}$ and $l = 10^{-3} \text{ m}$ (i and ii). The calculated

electric-field intensity of each of these samples on the illuminated face ($z = -75$ nm) at RCP illumination at the first CD peak—of 600 nm, 670 nm and 720 nm, respectively—is also shown (iii–v). **c,** Calculated g -factors of chiral nanoparticles corresponding to models 20–32, using chiral nanoparticles with various geometry changes: 20–22, chiral nanoparticles with increasing curvature; 23–26, chiral nanoparticles with aspect ratios of 1–3; 27–31, chiral nanoparticles with hollow structures constructed by removing cubic domains with side lengths of 70–130 nm; and 32, planar-triangle-based chiral nanoparticle with an edge length of 150 nm. The default size of chiral nanoparticles 20–31 is 150 nm.



Extended Data Fig. 9 | Effect of defects in the low-index-plane-exposed seeds on the morphology of 432 helicoid III. **a**, Characterization of twin boundary defects in seed nanoparticles. Twin boundaries were observed as bright lines in a single nanoparticle by scanning TEM imaging. Nanoparticles with a single twin and fivefold twins are indicated in red and yellow, respectively. **b**, Defect-induced morphology deformation of 432 helicoid III. SEM (left), TEM (middle) and selected-area electron diffraction (SAED; right) images are shown for an ideal 432 helicoid III (i), an irregular achiral nanoparticle (ii) and an irregular nanoparticle with broken 432 symmetry (iii). In the case of the irregular achiral particle (ii),

several diffraction spots that deviate from the regular diffraction pattern of the $\langle 100 \rangle$ zone (red) show polycrystalline character. In case of the particle with partially broken symmetry (iii), dark-field TEM images originating from diffraction spots 1 and 2 are also shown on the right, and demonstrate different crystallographic orientations in a single nanoparticle. We believe that the irregular, non-homogeneous shapes represented by ii and iii may originate from the twin boundary defects in seeds. By decreasing the population of twinned seeds, we expect that the g -factor can be further increased.



Extended Data Fig. 10 | Transmitted colour modulation by a dispersed solution of 432 helicoid III nanoparticles. **a, b,** Lorentz reciprocity of 432 helicoid III nanoparticles. The CD spectra of 432 helicoid III nanoparticles were measured from dispersion in aqueous solution (**a**) and deposition on a glass substrate (**b**). In both cases, CD measurements in the forwards and backwards directions produced identical responses. **c,** SEM images of 432 helicoid III nanoparticles with different sizes controlled by seed concentrations. Increasing the nanoparticle size resulted in a redshift in the plasmon resonance. The wavelengths at maximum CD intensity (λ_{\max}) are indicated in the images. **d,** Polarization-resolved transmittance spectra at different analyser angles. As the angle increased from -10° to 10° , transmittance at 550 nm gradually decreased, whereas that at 620 nm increased, resulting in a distinct asymmetric transition pattern. **e,** Colour

transition patterns of 432 helicoid III nanoparticles traced on CIE xy 1931 colour space (CIE, International Commission on Illumination). The white triangle indicates the RGB boundary. Each pattern shows elliptical traces with a clockwise rotational direction that reflects the asymmetric colour transition. **f,** CD spectra of a 432 helicoid III mixture. The spectral features of the broad and split CD peaks show linear superposition of the original components. **g,** Colour transition traces of the mixture on a colour space. The trace of the mixture was distinct from that of each original component and displays tailored colour transformation. **h,** Polarization-resolved transmission image of a 432 helicoid III mixture. Compared to the original components, the mixture shows different colour-transition patterns depending on the polarization angle.

Extended Data Table 1 | Comparison of *g*-factor for various chiral structures

	Structure	Wavelength	<i>g</i> -factor	Ref.
Amino acid and peptide	L-cysteine	215 nm	5×10^{-3}	this work
	L-glutathione	210 nm	2×10^{-4}	this work
	α -helical protein	190 nm	3×10^{-3}	44
Chiral molecule on achiral nanoparticle	Au nanoparticle coated with peptide	530 nm	3×10^{-4}	27
	Ag nanoparticle coated with assembled chiral supramolecule	530 nm	2×10^{-3}	45
	Nanogapped Au-Ag nanoparticle	430 nm	1×10^{-2}	46
Chiral arrangement of multiple nanoparticles	Au-Ag nanoparticle heterodimer with antibody-antigen bridge	400 nm	2×10^{-2}	47
	Au nanoparticle tetrahedral superstructure with DNA-nanoparticle conjugate	525 nm	2×10^{-2}	48
	Au nanoparticle helical superstructure with DNA origami bundle	700 nm	3×10^{-2}	9
	Au nanorod helical superstructure with bifacial DNA origami sheet	800 nm	2×10^{-2}	49
	Twisted Au nanorod dimer with reconfigurable DNA origami bundle	750 nm	2×10^{-2}	10
	Twisted Au nanorod oligomer with electrostatic side-by-side assembly	600 nm	7×10^{-2}	50
Chiral single nanoparticle	432 helicoid I	565 nm	3×10^{-2}	this work
	432 helicoid II	575 nm	5×10^{-2}	this work
	432 helicoid III	620 nm	2×10^{-1}	this work

Data are from this and previous^{9,10,27,44–50} work.